

ARMY RESEARCH LABORATORY



High-Speed Photographic Study of Wave Propagation and Impact Damage in Transparent Laminates

by Elmar Straßburger and M. O. Steinhauer

ARL-CR-605

April 2008

prepared by

Fraunhofer-Gesellschaft zur Förderung der angewandten Forschung e.V.
Leonrodstrasse 54, 80636
München, Germany

for

U.S. Army Research Laboratory
Aberdeen Proving Ground, MD

under contract

N62558-05-P-0303

NOTICES

Disclaimers

The findings in this report are not to be construed as an official Department of the Army position unless so designated by other authorized documents.

Citation of manufacturer's or trade names does not constitute an official endorsement or approval of the use thereof.

Destroy this report when it is no longer needed. Do not return it to the originator.

Army Research Laboratory

Aberdeen Proving Ground, MD 21005-5069

ARL-CR-605

April 2008

High-Speed Photographic Study of Wave Propagation and Impact Damage in Transparent Laminates

**Elmar Straßburger and M. O. Steinhauser
Weapons and Materials Research Directorate, ARL**

prepared by

**Fraunhofer-Gesellschaft zur Förderung der angewandten Forschung e.V.
Leonrodstrasse 54, 80636
München, Germany**

for

**U.S. Army Research Laboratory
Aberdeen Proving Ground, MD**

under contract

N62558-05-P-0303

REPORT DOCUMENTATION PAGE				Form Approved OMB No. 0704-0188
<p>Public reporting burden for this collection of information is estimated to average 1 hour per response, including the time for reviewing instructions, searching existing data sources, gathering and maintaining the data needed, and completing and reviewing the collection information. Send comments regarding this burden estimate or any other aspect of this collection of information, including suggestions for reducing the burden, to Department of Defense, Washington Headquarters Services, Directorate for Information Operations and Reports (0704-0188), 1215 Jefferson Davis Highway, Suite 1204, Arlington, VA 22202-4302. Respondents should be aware that notwithstanding any other provision of law, no person shall be subject to any penalty for failing to comply with a collection of information if it does not display a currently valid OMB control number.</p> <p>PLEASE DO NOT RETURN YOUR FORM TO THE ABOVE ADDRESS.</p>				
1. REPORT DATE (DD-MM-YYYY)	2. REPORT TYPE			3. DATES COVERED (From - To)
April 2008	Final			June 2005–July 2006
4. TITLE AND SUBTITLE				5a. CONTRACT NUMBER
High-Speed Photographic Study of Wave Propagation and Impact Damage in Transparent Laminates				N62558-05-P-0303
				5b. GRANT NUMBER
				5c. PROGRAM ELEMENT NUMBER
				5d. PROJECT NUMBER
				DC05
				5e. TASK NUMBER
				5f. WORK UNIT NUMBER
7. PERFORMING ORGANIZATION NAME(S) AND ADDRESS(ES)				8. PERFORMING ORGANIZATION REPORT NUMBER
Fraunhofer-Gesellschaft e.V. Hansasstrasse 27 c D 80686 München Germany		Fraunhofer-Institut für Kurzzeitdynamik Ernst-Mach-Institut Am Klingelberg 1 D-79588 Efringen-Kirchen Germany		ARL-CR-605
9. SPONSORING/MONITORING AGENCY NAME(S) AND ADDRESS(ES)				10. SPONSOR/MONITOR'S ACRONYM(S)
U.S. Army Research Laboratory ATTN: AMSRD-ARL-WM Aberdeen Proving Ground, MD 21005-5069				11. SPONSOR/MONITOR'S REPORT NUMBER(S)
12. DISTRIBUTION/AVAILABILITY STATEMENT				
Approved for public release; distribution is unlimited.				
13. SUPPLEMENTARY NOTES				
14. ABSTRACT				
Conventional transparent armor consists of glass laminates with polymer interlayer and backing. It has been demonstrated that the materials, the ratio of materials, and the type and thickness of the interlayers affect the ballistic efficiency of the laminate. Borosilicate glass, Starphire ultra-clear soda-lime glass, and the transparent, polycrystalline ceramic AION are materials being considered for transparent armor applications. A comprehensive series of Edge-on Impact tests has been conducted in order to examine wave and damage propagation through the single materials (baseline tests) and laminated structures.				
The numerical simulation part of this project focused on the modeling and simulation of projectile impact on the polycrystalline, transparent ceramic AION. In the approach chosen here, the ceramic was not treated as a continuum. In order to model the polyhedral microstructure of the ceramics, a code, which is based on the theory of power diagrams, was implemented. After having obtained a three-dimensional (3-D) grain structure that corresponds on average to what is observed in micrographs, these structures are being meshed in three dimensions using tetrahedra in 3-D vs. triangles in two dimensions. The generated and meshed microstructures were used as input for a commercial program package (LSDyna) and subsequent finite-element analyses.				
15. SUBJECT TERMS				
impact, glass, ceramics, photography, laminates				
16. SECURITY CLASSIFICATION OF:			17. LIMITATION OF ABSTRACT	18. NUMBER OF PAGES
a. REPORT UNCLASSIFIED			UL	64
b. ABSTRACT UNCLASSIFIED				
c. THIS PAGE UNCLASSIFIED			19a. NAME OF RESPONSIBLE PERSON James McCauley	
			19b. TELEPHONE NUMBER (Include area code) 410-306-0711	

Contents

List of Figures	iv
List of Tables	vii
1. Introduction	1
2. Experimental Set-up	1
3. Nomenclature	3
3.1 Fracture.....	3
3.2 Waves	5
4. Baseline Results	7
5. Starphire Glass Laminates	10
6. Influence of Interface Shape	15
7. Results With AlON	21
8. Numerical Simulations	23
8.1 Introduction	23
8.2 Generating Optimized Power Diagrams for FEM Analysis.....	25
8.3 Model, Results, and Discussion	32
8.4 Outlook (Numerical Simulation).....	35
9. Conclusion	37
10. References	38
Appendix. Complete Sets of High-Speed Photographs From Edge-on-Impact (EOI) Tests	41
Distribution List	48

List of Figures

Figure 1. EOI test set-up with Cranz-Schardin camera	2
Figure 2. Close-up view of test sample set-up for shadowgraphs	2
Figure 3. Typical damage pattern in float glass at $v_p \approx 50$ m/s; c_R = rayleigh wave velocity; c_T = transversal wave velocity; v_{Cr} = terminal crack velocity	3
Figure 4. Typical damage pattern in float glass at $v_p \approx 200$ m/s.....	4
Figure 5. Typical damage pattern with Starphire glass at $v_p \approx 400$ m/s.	4
Figure 6. Typical damage pattern in AlON at $v_p \approx 400$ m/s.	5
Figure 7. Shadowgraph (top) and corresponding crossed polarizers photograph (bottom) of Starphire specimen, 8.7 μ s after impact at ≈ 400 m/s.....	6
Figure 8. Selection of two shadowgraphs (top) and crossed polarizers photographs (bottom) from impact on Starphire glass with steel sphere at 440 m/s.....	7
Figure 9. Selection of two shadowgraphs (top) and crossed polarizers photographs (bottom) from impact on Starphire glass with steel cylinder at 390 m/s.	8
Figure 10. Selection of four shadowgraphs from impact on Borofloat glass with steel sphere at 430 m/s.....	9
Figure 11. Selection of two shadowgraphs (top) and crossed polarizers photographs (bottom) from impact on Borofloat glass with steel cylinder at 390 m/s.	9
Figure 12. Starphire laminates with interlayer of different thickness impacted by steel cylinder at 380 m/s.....	11
Figure 13. Selection of four shadowgraphs and corresponding crossed polarizers photographs; Starphire specimen with two PU bonding layers; impact velocity 404/395 m/s.....	12
Figure 14. Path-time history of wave propagation in specimens with two 2.54-mm polyurethane (DF) bonding layers.	13
Figure 15. Selection of four shadowgraphs and corresponding crossed polarizers photographs; Starphire specimen IM 500 bonding layer; impact velocity 388/399 m/s.	13
Figure 16. Path-time history of wave propagation in specimens with 0.64-mm IM 500 bonding layer.	14
Figure 17. Delay time vs. bonding layer thickness.	14
Figure 18. Interface types tested.	15
Figure 19. Selection of four shadowgraphs and corresponding crossed polarizers photographs; Starphire specimens with saw tooth interface; impact velocities 400/342 m/s.....	16
Figure 20. Path-time history of wave propagation in specimens with saw tooth shaped interface.....	16

Figure 21. Selection of four shadowgraphs and corresponding crossed polarizers photographs; Starphire specimens with corrugated interface; impact velocities 405/403 m/s.....	17
Figure 22. Path-time history of wave propagation in specimens with corrugated interface.....	17
Figure 23. Selection of four shadowgraphs and corresponding crossed polarizers photographs; Starphire specimens with wave shaped interface; impact velocities 384/404 m/s.....	18
Figure 24. Path-time history of wave propagation in specimens with wave shaped interface.....	19
Figure 25. Selection of four shadowgraphs from baseline test with thick Starphire specimen with straight interface; impact velocity 404 m/s.....	19
Figure 26. Schematic of EOI configuration to mimic impact on one tile of a ceramic mosaic.....	19
Figure 27. Complete set of high-speed photographs in crossed polarizers arrangement from EOI on intermediate glass layer, test no. 15726.	20
Figure 28. Photographs of target mount with AlON specimen (left) and mounted specimen between crossed (sheet) polarizers (right).	21
Figure 29. Selection of eight crossed polarizers photographs from test no. 15283 with steel confinement and impact velocity of 394 m/s.....	22
Figure 30. Path-time data of wave and fracture propagation in confined specimen, analysis of crossed polarizers photographs.....	23
Figure 31. Selection of four shadowgraphs and corresponding crossed polarizers photographs from baseline tests with AlON; spherical projectile; test nos. 15295–96.	24
Figure 32. Path-time history of wave and crack propagation in AlON from baseline tests with spherical projectile; test nos. 15295–96.....	24
Figure 33. Scheme for obtaining the grains' distribution from etched micrographs. In this scheme, an Al_2O_3 micrograph is shown.....	25
Figure 34. Available etched micrographs of aluminum oxynitride (AlON) (7). These micrographs were used to obtain optimized cell complex power diagrams in three dimensions.	26
Figure 35. Optimization scheme for our 3-D model to obtain a polyhedral grain structure which corresponds to the (only) 2-D structural information available from etched micrographs.....	26
Figure 36. Example of a generated initial (not yet optimized) 2-D cut of our 3-D cell complex.....	27
Figure 37. Optimization scheme for 3-D generated structures. We use the first three central moments for comparison of the generated structures with the distribution obtained from etched micrographs.	27
Figure 38. Efficiency of optimization procedure for AlON. After only 8 days of optimization, the coefficient χ^2 , which is a measure of the difference between the generated structure and the experimental data, is for all practical purposes very close to zero.....	28

Figure 39. Demonstration of the result of the optimization procedure for the area and perimeter distribution for Al_2O_3 . The Poisson distribution is the one obtained from a non-optimized initial power diagram. The optimized grain structures fit much better the experimental data.....	28
Figure 40. Generated and optimized 3-D grain structure of ALON. There is a total of 371 gr with a total of 130,000 elements in three dimensions. The grains are initially tied together by a contact force. Dimensions of the cube are arbitrary units as the size of the grains can be scaled to the desired size (in this case, $1 \times 1 \times 1$ mm).....	29
Figure 41. Direct comparison of a computer-generated granular surface (ALON) and a SEM picture of a typical ceramic grain structure, in this case Al_2O_3	29
Figure 42. The 2-D cut through a 3-D cell structure and subsequent meshing of the grains. Note that there are no intermediate elements (such as shell or interface elements) used in between the various grains. There is an initial contact force applied to the knots of adjacent interfaces of grains.....	30
Figure 43. Illustration of a mesh optimization procedure in two dimensions which removes short edges (and areas) such that a larger time step in a subsequent FEM analysis can be used.....	30
Figure 44. Illustration of different 3-D cuts through a generated power diagram. Structures with smooth edges or rough edges (leaving the surface grains unchanged) are possible.....	31
Figure 45. Another example of sample preparation from the raw data of the power diagram. Top: a view of the granular structure with different colors of grains for clarity. Bottom: the same structure but meshed with tetrahedral in three dimensions. Bottom right: another enlargement of a surface area exhibiting the meshed structure.....	31
Figure 46. Left: ALON plate LS-DYNA model, 8×8 mm, $0.3 \mu\text{s}$ after being hit by a steel sphere at 430 m/s . Right: same model after $0.6 \mu\text{s}$; the colors mark the pressure level -1 GPa to $+1 \text{ GPa}$; the blue line marks a zone where most contacts have already failed.....	32
Figure 47. Insufficiency of generic FEM approaches. A steel impactor hits an ALON tile. Red: failed elements. Starting configuration of an EOI at $v_p = 50 \text{ m/s}$	34
Figure 48. ALON modeled with SPH particles and a resolution of 1 mm. The result is different from the one in figure 47 (left), although all simulation conditions are the same.	34
Figure 49. Impacted ALON at 450 m/s with a steel impactor, $1.8 \cdot 10^{-7} \text{ s}$ after impact.....	35
Figure 50. Impacted ALON at 450 m/s with a steel impactor, $7.4 \cdot 10^{-7} \text{ s}$ after impact. Communition of the impact zone has already started.....	35
Figure 51. Impacted ALON at 450 m/s with a steel impactor, $4.9 \cdot 10^{-6} \text{ s}$ after impact. Failure of the ceramic with different fracture pattern propagating through the ceramic tile.....	36
Figure 52. Snapshot of an impact experiment with a spherical steel impactor and the magnified simulated 2-D sections of the ALON ceramic tile which exhibit the damage zone after the impact. The simulation model is a $7.8 \times 7.8 \text{-mm}^2$ section of the original $100 \times 100 \text{-mm}^2$ tile. Using an elastic plastic material model, the wave velocities in the experiment and in the simulations are the same. The simulation snapshot is taken after the shock wave has crossed about 70% of the simulated part of the tile. Displayed minimum and maximum pressure is $\pm 1 \text{ GPa}$	36

Figure A-1. Complete set of high-speed photographs from EOI test of laminated Starphire specimen with saw tooth interface, shadowgraph configuration; test no. 15724	42
Figure A-2. Complete set of high-speed photographs from EOI test of laminated Starphire specimen with saw tooth interface, crossed polarizers configuration; test no. 15725	43
Figure A-3. Complete set of high-speed photographs from EOI test of laminated Starphire specimen with corrugated interface, shadowgraph configuration; test no. 15727.....	44
Figure A-4. Complete set of high-speed photographs from EOI test of laminated Starphire specimen with corrugated interface, crossed polarizers configuration; test no. 15728.	45
Figure A-5. Complete set of high-speed photographs from EOI test of laminated Starphire specimen with wave shaped interface, shadowgraph configuration; test no. 15731.	46
Figure A-6. Complete set of high-speed photographs from EOI test of laminated Starphire specimen with wave shaped interface, crossed polarizers configuration; test no. 15730.....	47

List of Tables

Table 1. Measured wave, crack, and damage velocities with Starphire soda-lime glass.	10
Table 2. Measured wave, crack, and damage velocities with Borofloat glass.....	10
Table 3. Tests with laminated Starphire glass.	11
Table 4. Compilation of experimental parameters from tests with differently shaped interfaces.....	15
Table 5. Tests with AlON.	21

INTENTIONALLY LEFT BLANK.

1. Introduction

Conventional transparent armor consists of glass laminates with polymer interlayer and backing. It has been demonstrated that the materials, the ratio of materials, and the type and thickness of the interlayers affect the ballistic efficiency of the laminate.

Borosilicate glass, Starphire* ultra-clear soda-lime glass, and the transparent, polycrystalline ceramic AlON are materials being considered for transparent armor applications. A comprehensive series of Edge-on Impact (EOI) tests has been conducted in order to examine wave and damage propagation through the single materials (baseline tests) and laminated structures.

The numerical simulation part of this project focused on the modeling and simulation of projectile impact on the polycrystalline, transparent ceramic AlON. In the approach chosen here, the ceramic was not treated as a continuum. In order to model the polyhedral microstructure of the ceramics, a code, which is based on the theory of power diagrams, was implemented. After having obtained a three-dimensional (3-D) grain structure that corresponds on average to what is observed in micrographs, these structures are being meshed in 3-Ds using tetrahedra in 3-D vs. triangles in two dimensions. The generated and meshed microstructures are used as input for a commercial program package (LSDyna) and subsequent finite-element (FE) analyses.

2. Experimental Set-up

The EOI test method coupled with a high-speed Cranz-Schardin camera, with frame rates up to 10^7 fps, has been applied in order to visualize damage propagation and dynamic fracture in structural ceramics. Two different optical configurations were employed. A regular transmitted light shadowgraph set-up was used to observe wave and damage propagation and a modified configuration, where the specimens were placed between crossed polarizers and the photo-elastic effect was utilized to visualize the stress waves. Pairs of impact tests at approximately equivalent velocities were carried out in transmitted plane (shadowgraphs) and crossed polarized light. Figure 1 shows a schematic of the EOI test with the added crossed polarizers; figure 2 illustrates an exploded view of the impactor/sample interaction.

* Starphire is a registered trademark of PPG, Pittsburgh, PA.

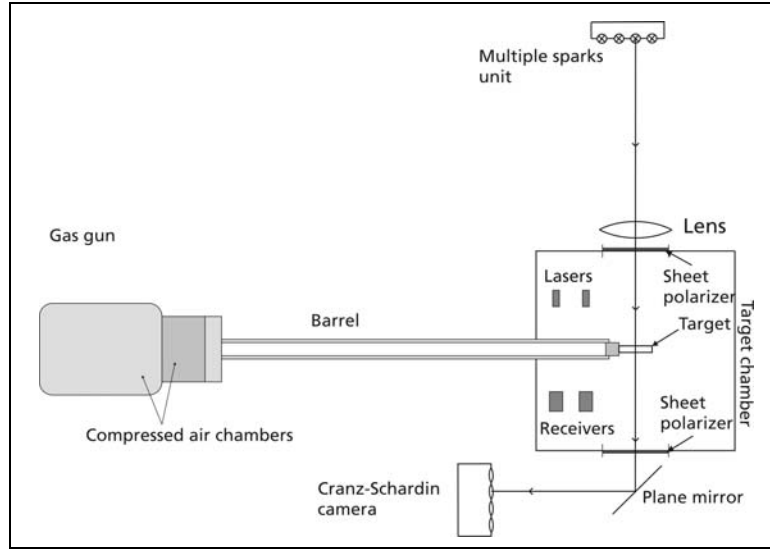


Figure 1. EOI test set-up with Cranz-Schardin camera.

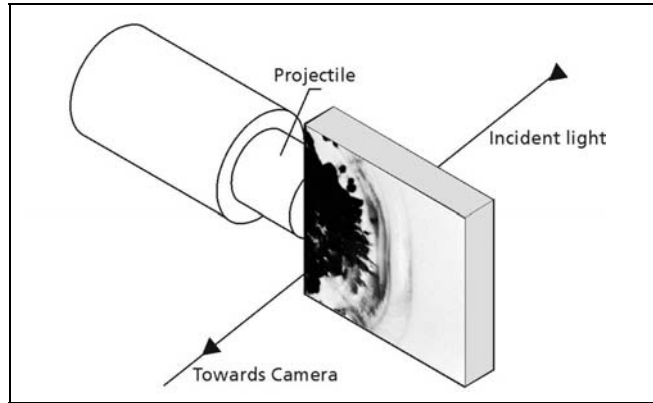


Figure 2. Close-up view of test sample set-up for shadowgraphs.

Both steel solid cylinder and spherical impactors have been used at velocities from 350 to 450 m/s on 100- × 100- × 10-mm plates. Once the baseline glass materials were tested and analyzed, multi-component glass laminates were produced and tested at ≈ 400 m/s. The data collected from the EOI test consists of a series of 20 photographs as a function of time, typically at 0.25–2 μ s intervals. Pairs of impact tests at approximately equivalent velocities are carried out in plane and crossed polarized light to correlate the dynamic fracture with the associated stress fields. Detailed graphs are then created plotting crack, damage, and compression and shear stress wave velocities. More details on the set-up can be found in the first interim report (1).

3. Nomenclature

Since two different methods (shadowgraphs, crossed polarizers) were employed for the visualization of wave and damage propagation, where not only the stress waves appear in different forms, but also different types of fracture can be distinguished, it is necessary to clarify the designations of the various phenomena.

3.1 Fracture

The nomenclature for the different fracture types and patterns was defined in earlier EOI studies (2) and is also used in the work reported here. Figures 3 and 4 illustrate typical damage patterns observed with soda-lime glass at low (~ 50 m/s) and medium (~ 200 m/s) impact velocities.

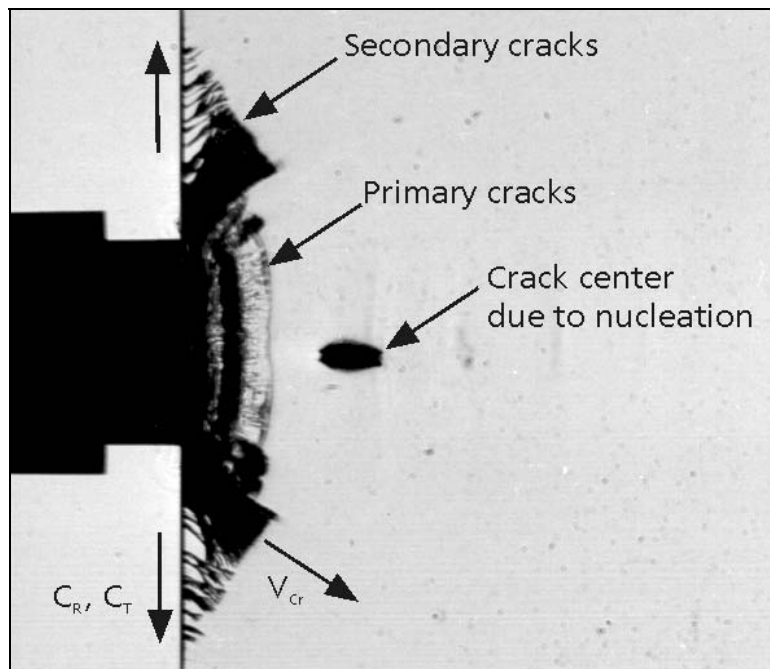


Figure 3. Typical damage pattern in float glass at $v_p \approx 50$ m/s;
 c_R = rayleigh wave velocity; c_T = transversal wave velocity;
 v_{cr} = terminal crack velocity.

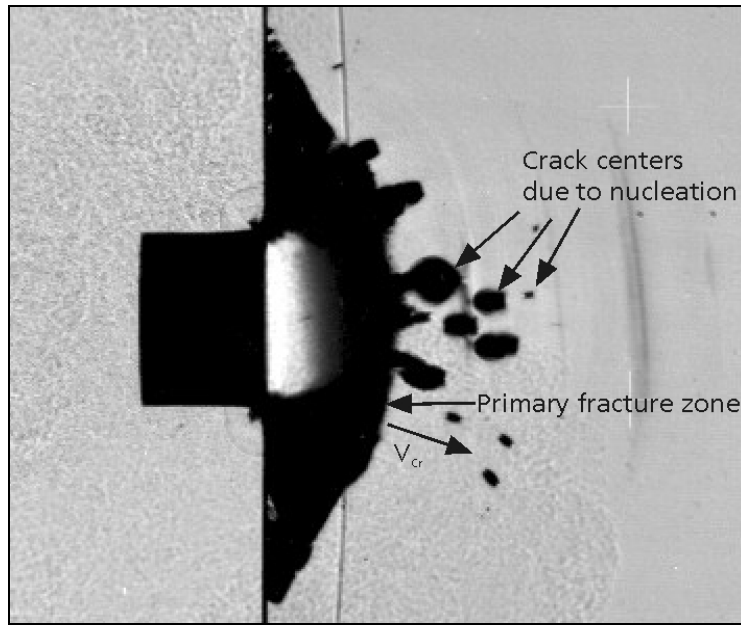


Figure 4. Typical damage pattern in float glass at $v_p \approx 200$ m/s.

While figure 5 illustrates the typical damage pattern in Starphire high-purity soda-lime glass at an impact velocity of ≈ 400 m/s, figure 6 shows the damage pattern in AlON, transparent, polycrystalline ceramic at about the same impact velocity.

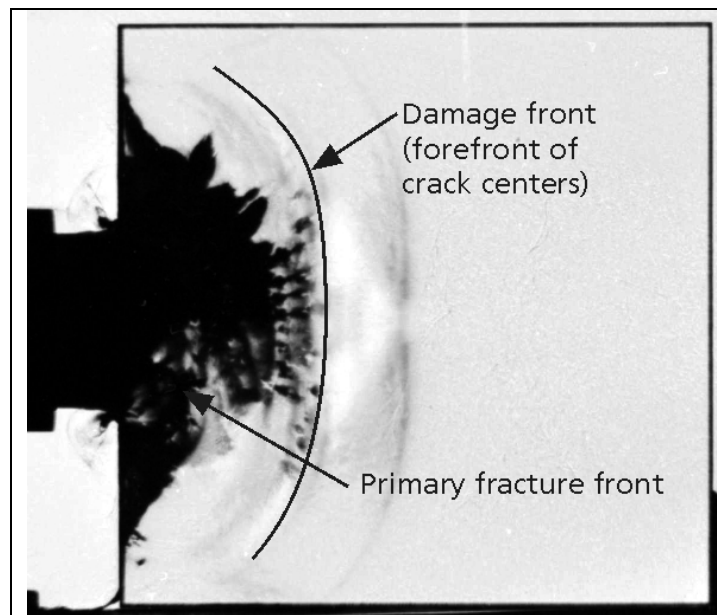


Figure 5. Typical damage pattern with Starphire glass at $v_p \approx 400$ m/s.

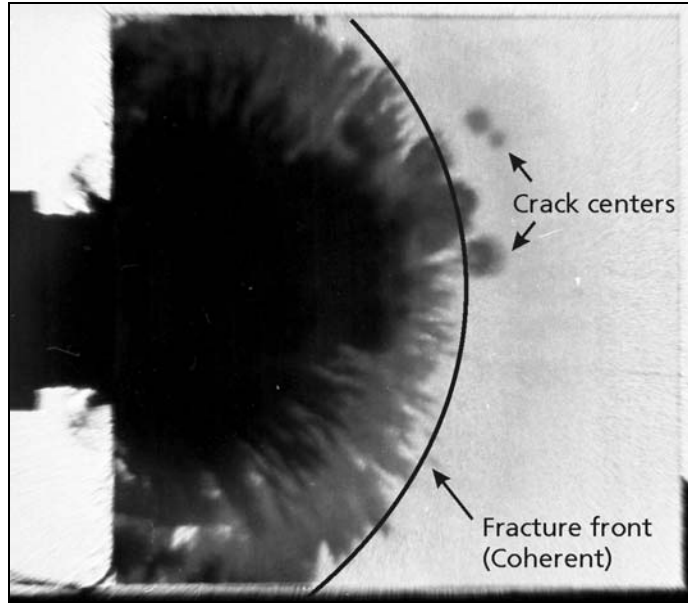


Figure 6. Typical damage pattern in AlON at $v_p \approx 400$ m/s.

3.2 Waves

The two different optical techniques employed exhibit different sensitivities with respect to the stress level that can be visualized. In a shadowgraph image, the light intensity depends on the second spatial derivative $\partial^2 n / \partial x^2$ of the refractive index, whereas in the crossed polarizers set-up, the intensity of the transmitted light depends on the photo-elastic properties of the material. Therefore, it is possible that the first visible wave front in the shadowgraph configuration appears at a different position than the forefront of the stress wave, visible in the crossed polarizers set-up. Both techniques can visualize different parts of the same stress wave. This is demonstrated in figure 7, which shows the shadowgraph and the corresponding crossed polarizers photograph of a Starphire specimen at 8.7 μ s after impact.

The width of the stress wave can be estimated from the length of the projectile and the longitudinal wave speed in the projectile and target material. When the projectile hits the target, a wave is generated not only in the target but also in the projectile. The maximum length of the stress pulse is given by the time the wave needs to travel once through the projectile and back. The thickness of the solid cylindrical part of the projectile was 8 mm. With a longitudinal wave speed of 5100 m/s in steel, this yields a stress pulse length of

$$\Delta t_{\text{stress}} \approx 2 \cdot \frac{8 \text{ mm}}{5.1 \frac{\text{mm}}{\mu\text{s}}} = 3.1 \mu\text{s}. \quad (1)$$

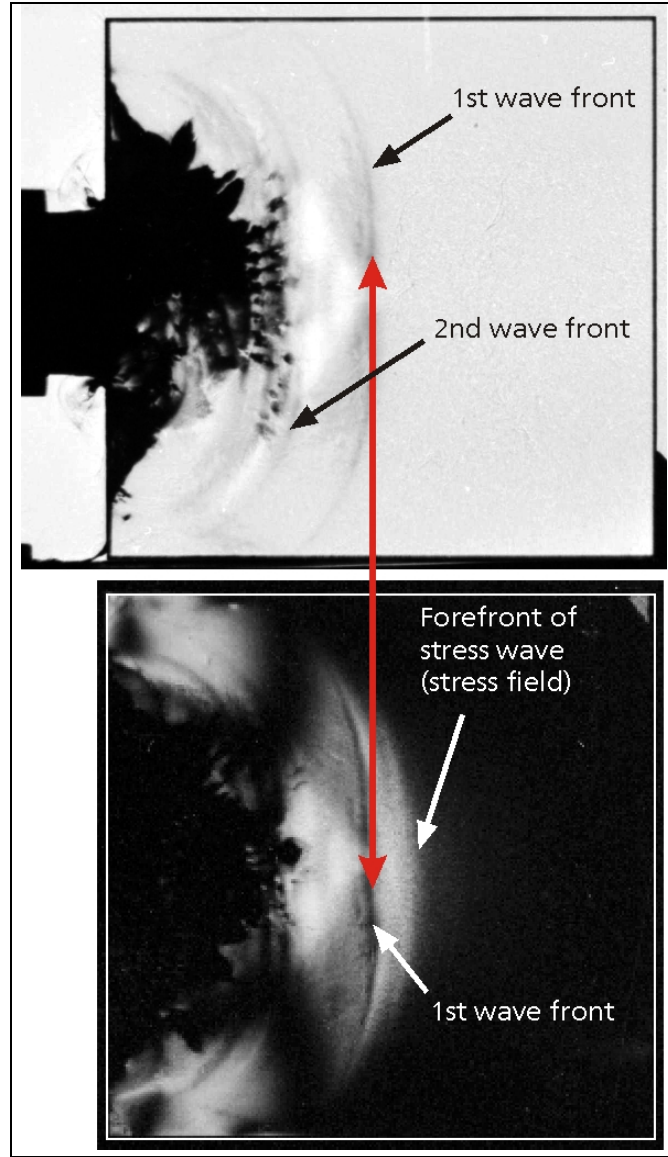


Figure 7. Shadowgraph (top) and corresponding crossed polarizers photograph (bottom) of Starphire specimen, 8.7 μ s after impact at ≈ 400 m/s.

Release waves from the edges of the projectile are neglected in this estimate. The longitudinal wave velocity in Starphire glass is ≈ 5800 m/s. Therefore, the maximum spatial width of the stress wave in the target can be

$$\Delta s_{\text{stress}} \approx 3.1 \mu\text{s} \cdot 5.8 \frac{\text{mm}}{\mu\text{s}} \approx 18 \text{ mm} . \quad (2)$$

The formation of the second wave front is caused by the geometry of the specimens and is due to the initiation and superposition of waves, generated at the side surfaces of the specimens. The distance to the first wave front depends on the thickness and Poisson's ratio (2).

4. Baseline Results

Experiments performed in plane light show the evolution of damage and material failure, while the photoelastic visualization illustrates the stress wave propagation as a function of time.

Figure 8 shows a selection of two shadowgraphs (top) and corresponding crossed polarizers photographs (bottom) of a baseline test with Starphire glass, impacted by a spherical steel projectile with a 16 mm diameter at 440 m/s. The shadowgraphs show a crack front growing from the impacted edge of the specimen. Only one crack center can be observed close to the upper edge of the specimen. The crossed polarizers photographs illustrate the propagation of the longitudinal and the transversal stress waves. Release waves due to reflections at the upper and lower edge can also be recognized. Note that damage appears dark on the shadowgraphs and the zones with stress birefringence are exhibited as bright zones in the crossed polarizers photographs.

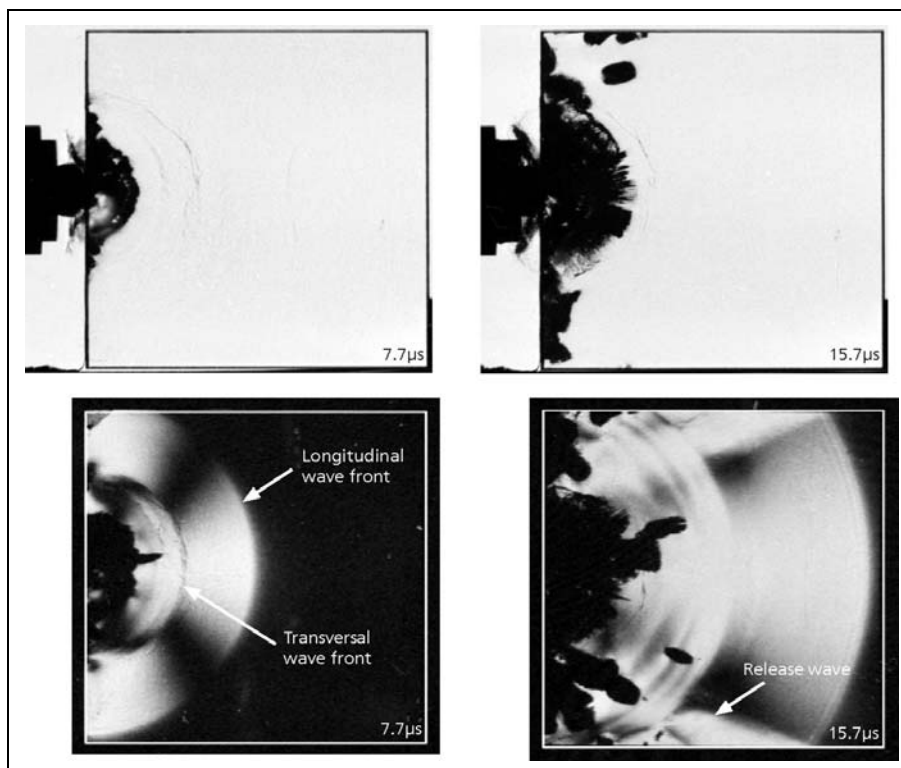


Figure 8. Selection of two shadowgraphs (top) and crossed polarizers photographs (bottom) from impact on Starphire glass with steel sphere at 440 m/s.

Figure 9 shows a selection of two shadowgraphs along with the corresponding crossed polarizers photographs of the baseline tests with the cylindrical projectile. A coherent damage zone is growing from the impacted edge, preceded by a zone with separated crack centers, initiated by the stress waves. It can be recognized that the stress wave front appears more advanced and exhibits a different curvature in the crossed polarizers view. This seeming discrepancy can be explained by the different sensitivities that the different optical techniques employed exhibit with respect to the stress level that can be visualized. In a shadowgraph image, the light intensity depends on the second spatial derivative $\partial^2 n / \partial x^2$ of the refractive index, whereas in the crossed polarizers set-up, the intensity of the transmitted light depends on the photo-elastic properties of the material. Therefore, it is possible that the first visible wave front in the shadowgraph configuration appears at a different position than the forefront of the stress wave, visible in the crossed polarizers set-up. Both techniques can visualize different parts of the same stress wave.

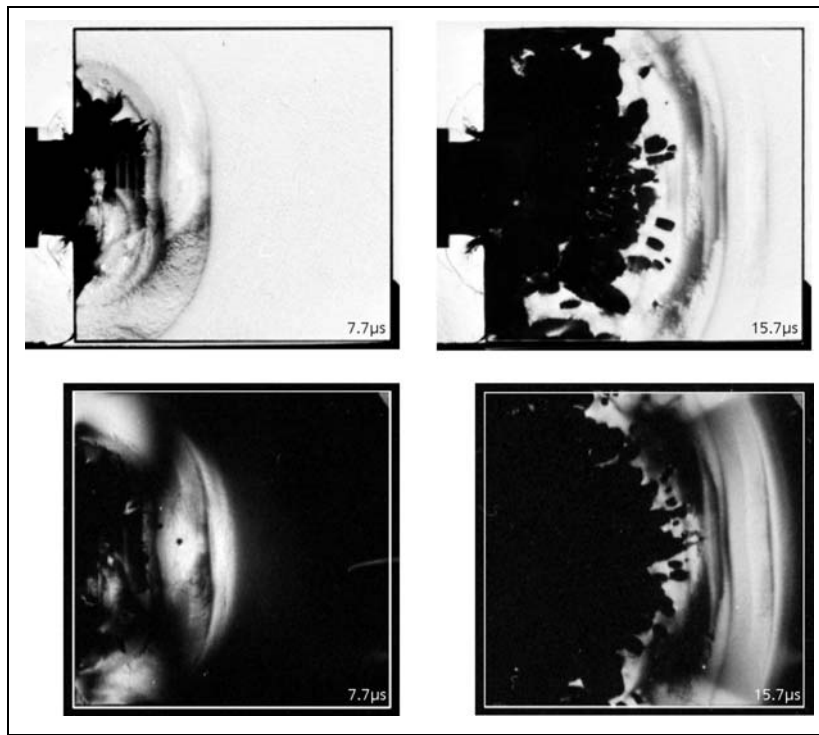


Figure 9. Selection of two shadowgraphs (top) and crossed polarizers photographs (bottom) from impact on Starphire glass with steel cylinder at 390 m/s.

The high-speed photographs from baseline tests with the steel sphere and cylinder on Borofloat* glass are presented in figures 10 and 11. Crack and damage patterns very similar to those observed with soda-lime glass can be recognized. However, the crack and damage velocities determined from the position-time analysis of the high-speed photographs were higher than with

* Borofloat is a registered trademark of Schott North America, Inc., Elmsford, NY.

Starphire glass. Tables 1 and 2 summarize the crack velocity, damage velocity, and wave propagation data of the baseline tests with Starphire and Borofloat glass, respectively.

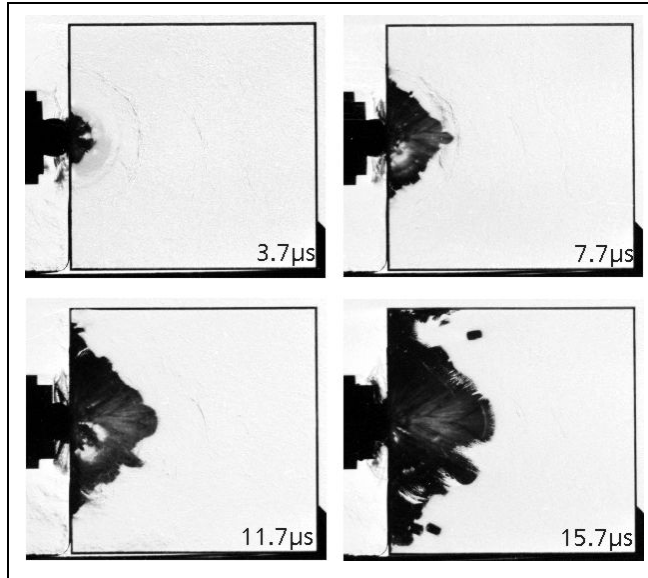


Figure 10. Selection of four shadowgraphs from impact on Borofloat glass with steel sphere at 430 m/s.

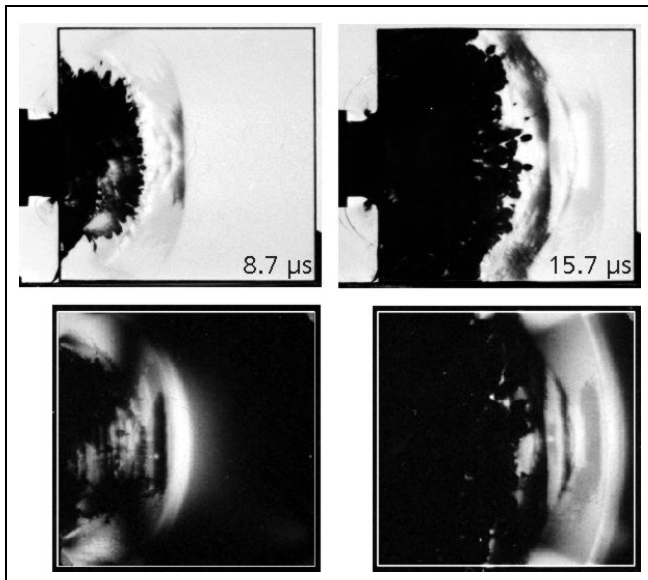


Figure 11. Selection of two shadowgraphs (top) and crossed polarizers photographs (bottom) from impact on Borofloat glass with steel cylinder at 390 m/s.

Table 1. Measured wave, crack, and damage velocities with Starphire soda-lime glass.

Impactor	Optical Set-up	Long. Wave Velocity c_L (m/s)	Trans. Wave Velocity c_T (m/s)	Crack Velocity v_{Cr} (m/s)	Damage Velocity v_D (m/s)
Sphere	Shadowgraph	—	—	1580	1580
Sphere	Crossed polarizers	5763	3518	—	—
Cylinder	Shadowgraph	5761	—	—	3270
Cylinder	Crossed polarizers	5779	—	—	—

Table 2. Measured wave, crack, and damage velocities with Borofloat glass.

Impactor	Optical Set-up	Long. Wave Velocity c_L (m/s)	Trans. Wave Velocity c_T (m/s)	Crack Velocity v_{Cr} (m/s)	Damage Velocity v_D (m/s)
Sphere	Shadowgraph	5462	—	2034	2034
Cylinder	Shadowgraph	5531	—	—	4150
Cylinder	Crossed polarizers	5635	—	—	—

5. Starphire Glass Laminates

The influence of a polyurethane (PU) bonding layer on wave and damage propagation was examined with cylindrical projectiles only. Four pairs of tests with specimens consisting of two parts of the dimensions $50 \times 100 \times 9.5$ mm were conducted in order to examine the influence of interlayer thickness. Starphire specimens with bonding layers of thickness 0.64, 1.27, 2.54, and 5.08 mm were examined. The influence of two PU bonding layers was tested with specimens that were built of three parts of the dimensions $30 \times 100 \times 9.5$ mm.

One pair of tests was conducted with a different type of PU interlayer, designated IM 500. Table 3 shows a compilation of these tests.

The phenomenology of damage and wave propagation in Starphire laminates has already been discussed in the first and second Interim Report (1, 3). Therefore, a summary of these results will be given in the following section. Only the results with the IM 500 type bonding layer will be shown in detail.

Figure 12 illustrates a comparison of wave propagation and damage in Starphire specimens with bonding layers of thickness 0.64, 2.54, and 5.08 mm. The impact velocity was 380 ± 5 m/s in all tests. The upper line of pictures shows the shadowgraphs, while the corresponding crossed polarizers photographs are presented in the lower line of pictures, respectively. Figure 12a illustrates the specimens at $10.7 \mu s$ and figure 12b at $23.7 \mu s$ after projectile impact. The shadowgraphs at $10.7 \mu s$ show that the first glass layer (left part of specimen) is damaged

Table 3. Tests with laminated Starphire glass.

Test No.	Interlayer (in)	Impact Velocity (m/s)	Optical Set-up	Time Intervals Picture No.: Δt (μs)
15274	0.025 DF	375	Shadowgraph	1-14: 1; 14-20: 2 μs
15275	0.025 DF	387	Crossed polarizers	1-14: 1; 14-20: 2 μs
15299	0.050 DF	389	Shadowgraph	1-14: 1; 14-20: 2 μs
15300	0.050 DF	395	Crossed polarizers	1-14: 1; 14-20: 2 μs
15273	0.100 DF	384	Shadowgraph	1-16: 1; 16-20: 2 μs
15280	0.100 DF	382	Crossed polarizers	1-16: 1; 16-20: 2 μs
15278	0.200 DF	385	Shadowgraph	1-10: 1; 10-20: 2 μs
15279	0.200 DF	384	Crossed polarizers	1-10: 1; 10-20: 2 μs
15309	2 × 0.100 DF	404	Shadowgraph	1-8: 2; 8-16: 1; 16-20: 2
15310	2 × 0.100 DF	395	Crossed polarizers	1-8: 2; 8-16: 1; 16-20: 2
15307	0.100 IM 500	388	Shadowgraph	1-4: 2; 4-8: 1; 8-20: 2
15308	0.100 IM 500	399	Crossed polarizers	1-4: 2; 4-8: 1; 8-20: 2

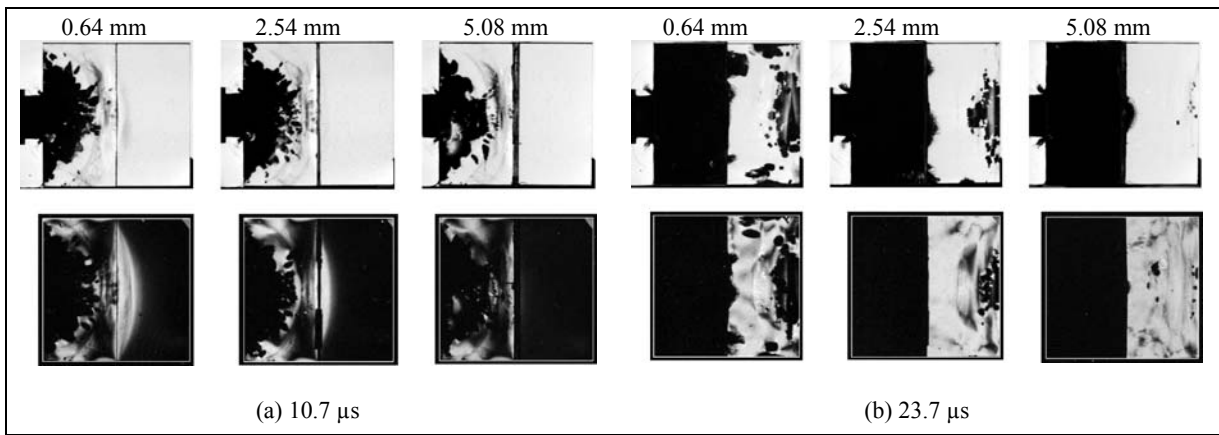


Figure 12. Starphire laminates with interlayer of different thickness impacted by steel cylinder at 380 m/s.

through the coherent fracture front growing from the impacted edge and through the nucleation of crack centers, initiated by the longitudinal stress waves. At that time, no damage can be recognized in the second glass layer (right part of specimen). The crossed polarizers photographs demonstrate that the first longitudinal stress pulse has not yet crossed the thickest glue interlayer (right), whereas the stress wave is clearly visible in the right half of the specimens with the thinner glue interlayer.

After 23.7 μs (figure 7b), the compressive stress pulse has already been reflected as a tensile wave at the rear edge of the specimens in all three cases. The shadowgraphs illustrate that damage in the second glass layer is mainly due to the tensile wave and starts from the rear edge of the specimen. In the case of the thickest glue interlayer, only little damage was observed in the second glass layer.

The effect of two bonding layers of 2.54 mm thickness is demonstrated in figure 13 which shows a selection of four shadowgraphs and corresponding crossed polarizers photographs in the time interval from 6 to 25 μ s after impact of a steel cylinder at about 400 m/s. The first layer of glass was completely damaged within the first 15 μ s. Damage could be recognized in the second layer after 16 μ s, when the first crack centers became visible which were initiated by the reflection of the compression wave at the interface between the second glass and the second bonding layer. No damage was observed in the third glass layer during the time interval of observation.

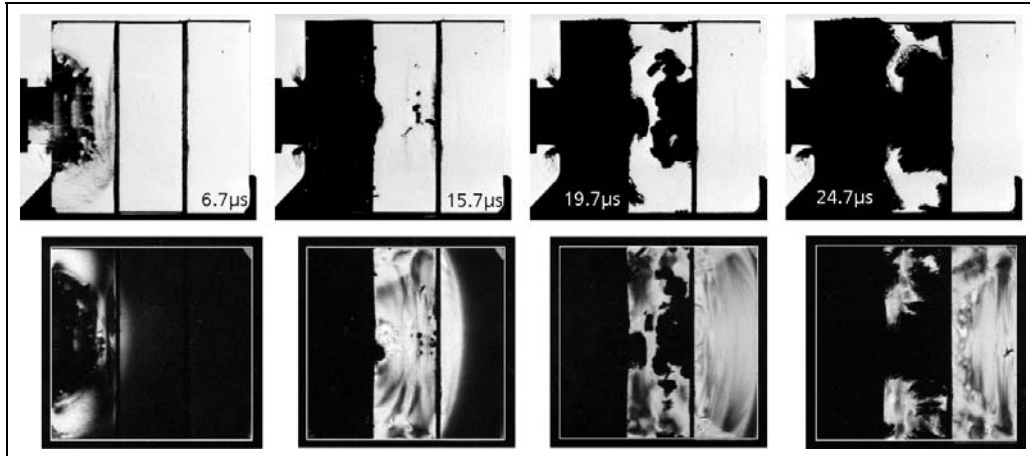


Figure 13. Selection of four shadowgraphs and corresponding crossed polarizers photographs; Starphire specimen with two PU bonding layers; impact velocity 404/395 m/s.

The wave propagation in the specimens was analyzed and the path-time history for the case with the two 2.54-mm bonding layers is presented in figure 14.

The results with an aliphatic PU bonding layer of type IM 500 and a nominal thickness of 0.64 mm are shown in figure 15 (selection of high-speed photographs) and figure 16 (path-time history of wave propagation).

The high-speed photographs in figure 15 illustrate that the damage formation in the second glass layer is similar to the case with the DF polyurethane bonding layer of the same thickness.

When the waves hit an interlayer, one part is reflected while the other part is transmitted into the next glass layer. Due to the low acoustic impedance of the interlayer compared to the glass, the amplitude of the stress pulses is attenuated considerably. The low wave velocity in the interlayers effected a time delay at each bonding layer compared to the unperturbed propagation through the glass.

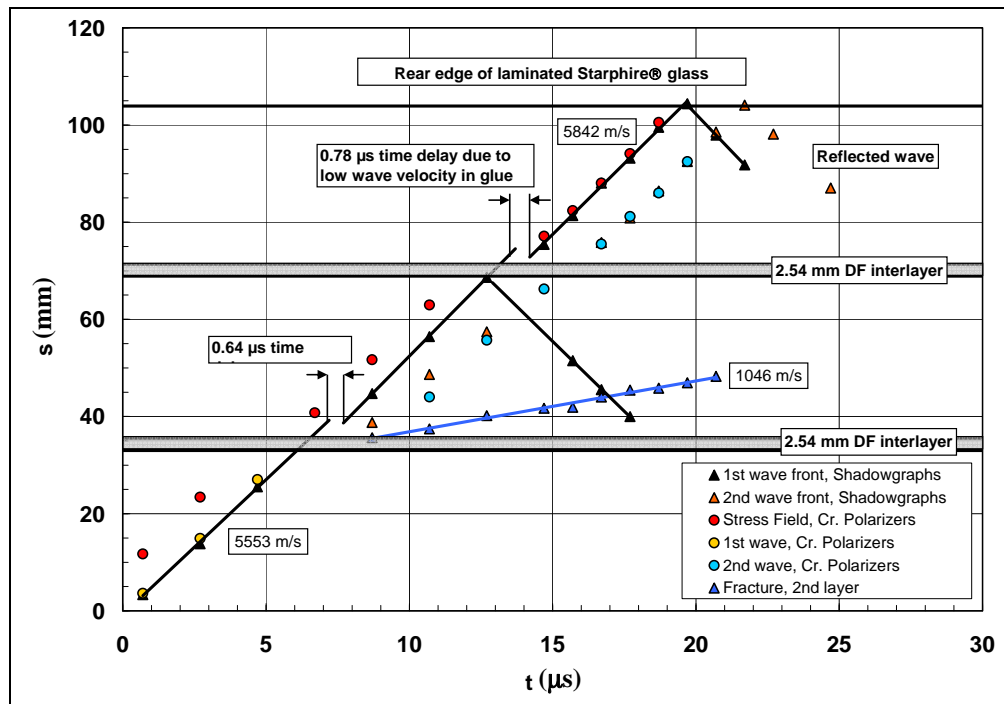


Figure 14. Path-time history of wave propagation in specimens with two 2.54-mm polyurethane (DF) bonding layers.

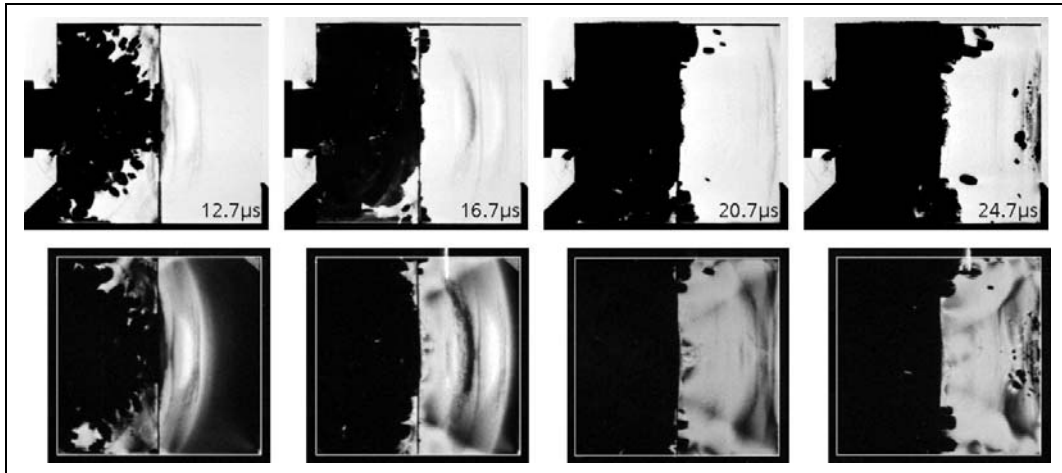


Figure 15. Selection of four shadowgraphs and corresponding crossed polarizers photographs; Starphire specimen IM 500 bonding layer; impact velocity 388/399 m/s.

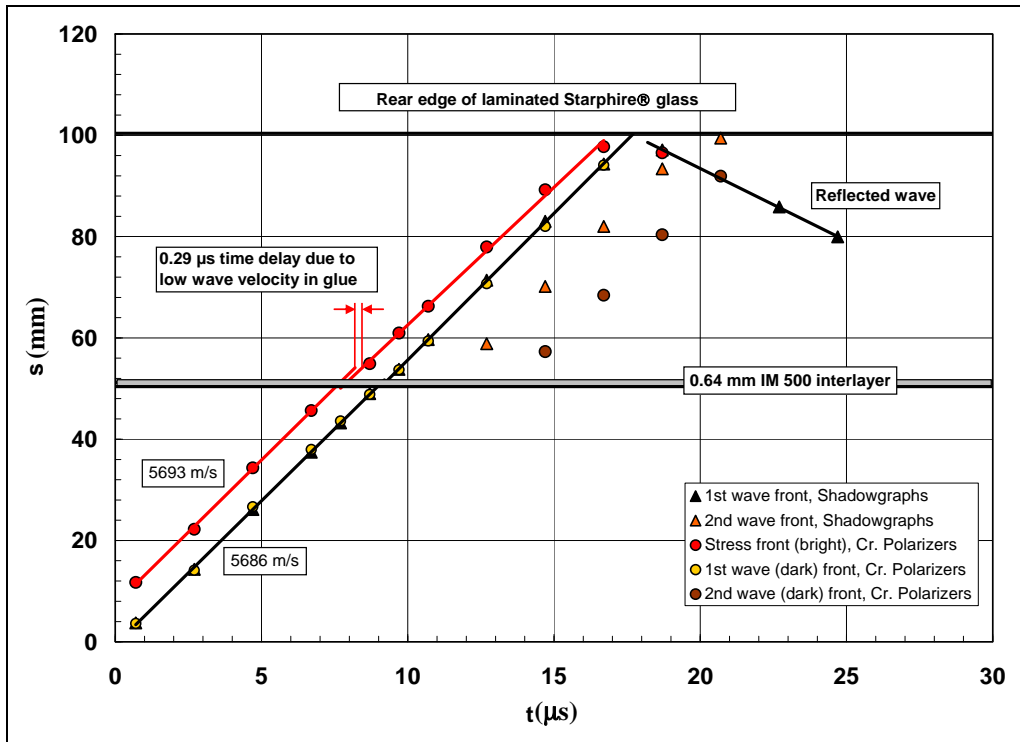


Figure 16. Path-time history of wave propagation in specimens with 0.64-mm IM 500 bonding layer.

The delay times measured in all tests were plotted in a delay time versus bonding layer thickness diagram (figure 17). Linear regression of the data yielded an average delay time of $0.33 \mu\text{s/mm}$. This is in good agreement with the calculated value based on a longitudinal wave velocity $c_L = 5770 \text{ m/s}$ for Starphire glass and $c_L \approx 2000 \text{ m/s}$ for the polyurethane (4).

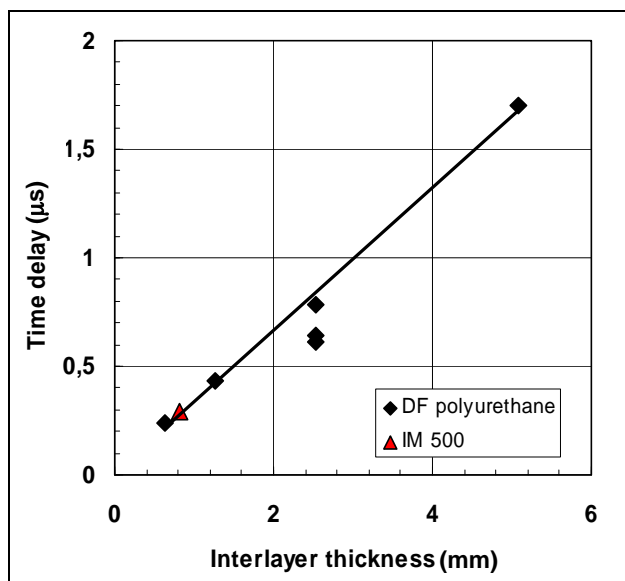


Figure 17. Delay time vs. bonding layer thickness.

6. Influence of Interface Shape

A series of EOI-tests was performed in order to study the influence of the shape of the interface between Starphire glass layers on wave and damage propagation. Three different types of interface were considered: saw tooth, corrugated, and wave shape. The different interface types are illustrated in figure 18. The contour of the wave shape interface was adopted from the contours observed in the baseline tests (crossed polarizers) with Starphire glass. One additional baseline test with a straight interface was conducted with a Starphire specimen of 12.3-mm thickness. Table 4 shows a compilation of experimental parameters from this test series.

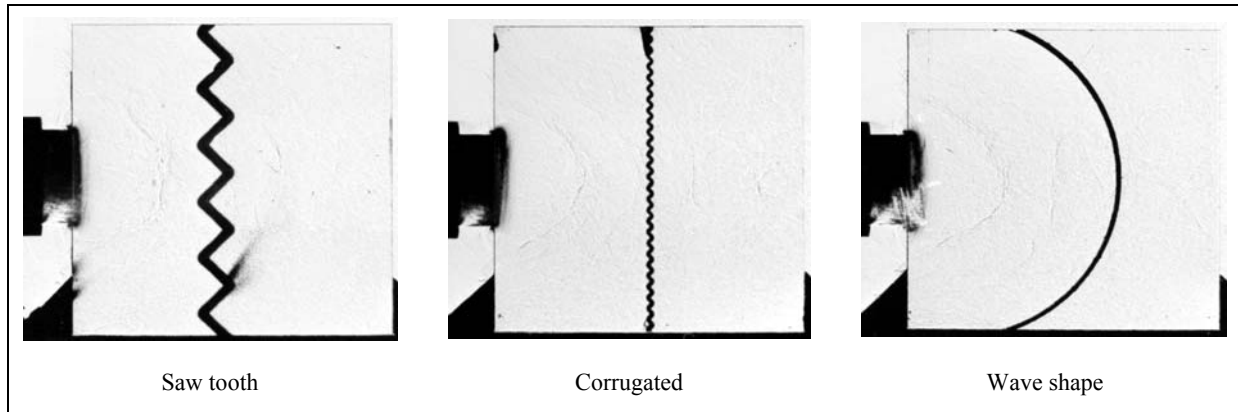


Figure 18. Interface types tested.

Table 4. Compilation of experimental parameters from tests with differently shaped interfaces.

Test No.	Interface		Imp. Velocity (m/s)	Optical Set-up	Time intervals Picture No.: Δt (μs)
	Type	DF Thickness (mm)			
15724	Saw tooth	3.9	400	Shadowgraph	1-14: 1 μs; 14-20: 2 μs
15725	Saw tooth	3.9	342	Crossed polarizers	1-14: 1 μs; 14-20: 2 μs
15727	Corrugated	1.3	405	Shadowgraph	1-14: 1 μs; 14-20: 2 μs
15728	Corrugated	1.3	403	Shadowgraph	1-14: 1 μs; 14-20: 2 μs
15729	Straight	3.5	404	Shadowgraph	1-14: 1 μs; 14-20: 2 μs
15730	Wave shape	1.8	384	Crossed polarizers	1-14: 1 μs; 14-20: 2 μs
15731	Wave shape	1.8	404	Shadowgraph	1-7: 2 μs; 7-17: 0.5 μs 17-20: 1 μs

Figure 19 shows a selection of four shadowgraphs along with the corresponding crossed polarizers photographs of the tests with the saw tooth interface. The complete sets of high-speed photographs are presented in figures A-1 and A-2 in the appendix.

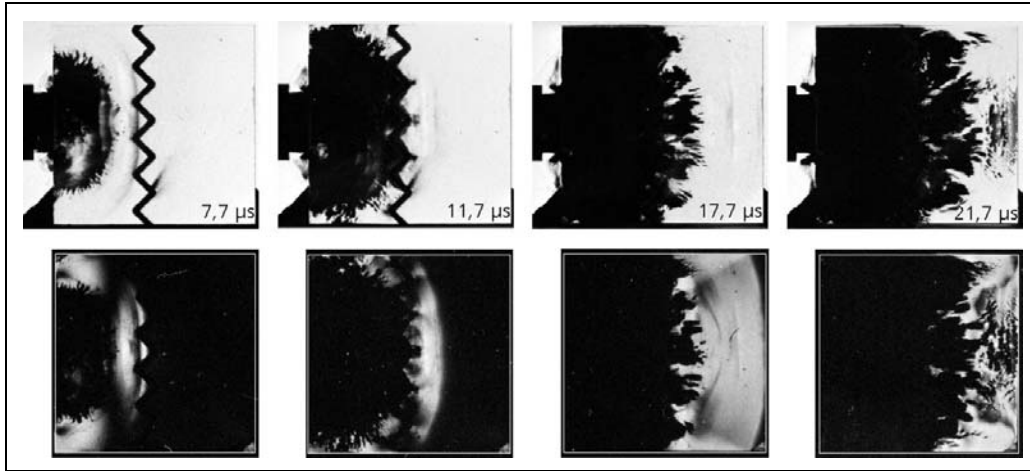


Figure 19. Selection of four shadowgraphs and corresponding crossed polarizers photographs; Starphire specimens with saw tooth interface; impact velocities 400/342 m/s.

In contrast to the results of all tests with straight interfaces damage by nucleation of crack centers can be observed in the second layer, before the stress wave is reflected at the rear edge. Shortly after the stress wave has crossed the interface, cracks can be recognized, initiated especially at the tips of the saw tooth interface. The path-time history of wave and damage propagation is depicted in figure 20. The best fit straight line (dashed) through the nucleation sites of three leading crack centers yields a damage velocity of 4256 m/s in the second glass layer.

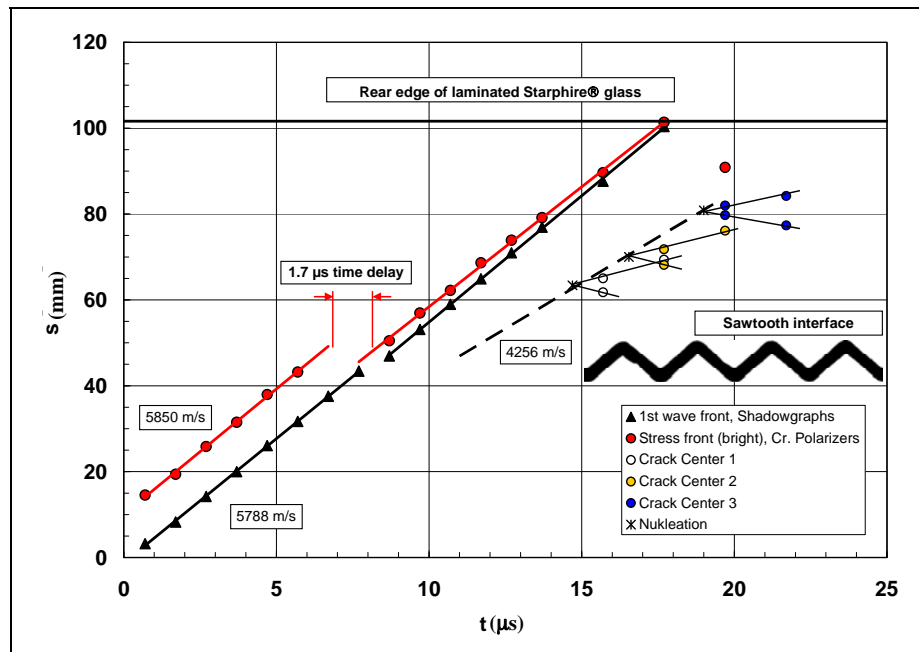


Figure 20. Path-time history of wave propagation in specimens with saw tooth shaped interface.

Figure 21 shows a selection of four shadowgraphs along with the corresponding crossed polarizers photographs of the tests with the corrugated interface. The complete sets of high-speed photographs are presented in figures A-3 and A-4 in the appendix.

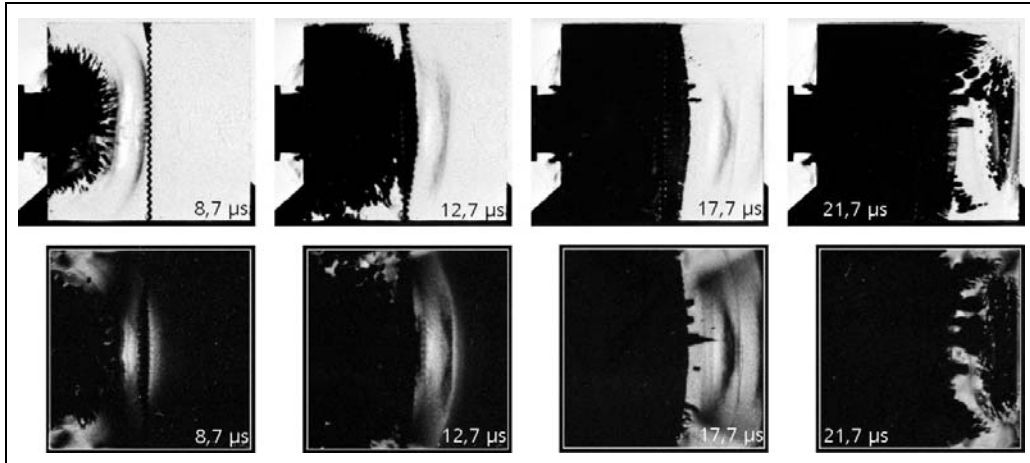


Figure 21. Selection of four shadowgraphs and corresponding crossed polarizers photographs; Starphire specimens with corrugated interface; impact velocities 405/403 m/s.

The sequence of high-speed photographs shows that cracks are initiated all along the interface, which form a dense crack front, propagating at the terminal crack speed of 1524 m/s in Starphire glass (see figure 22). The crack front in the second glass layer is preceded by several crack centers, nucleated by the stress wave, before it is reflected at the rear edge of the specimen. The path-time history of wave and damage propagation is depicted in figure 22.

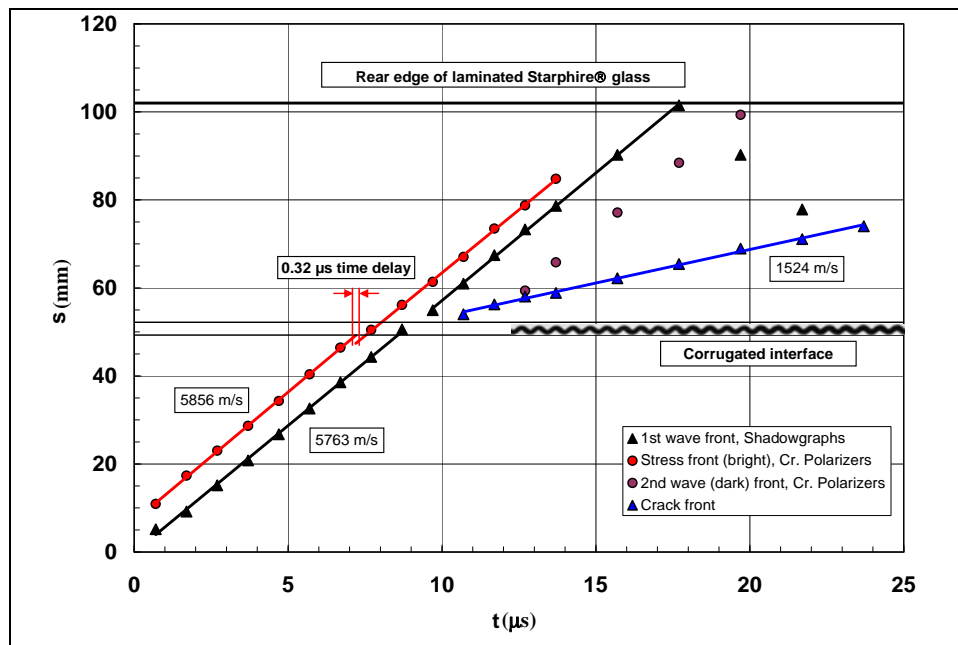


Figure 22. Path-time history of wave propagation in specimens with corrugated interface.

A selection of four shadowgraphs along with the corresponding crossed polarizers photographs of the tests with the wave shaped interface is depicted in figure 23. Note that the time intervals chosen in the test with the crossed polarizers were different from those in the test with the shadowgraph arrangement. The complete sets of high-speed photographs are presented in figures A-5 and A-6 in the appendix.

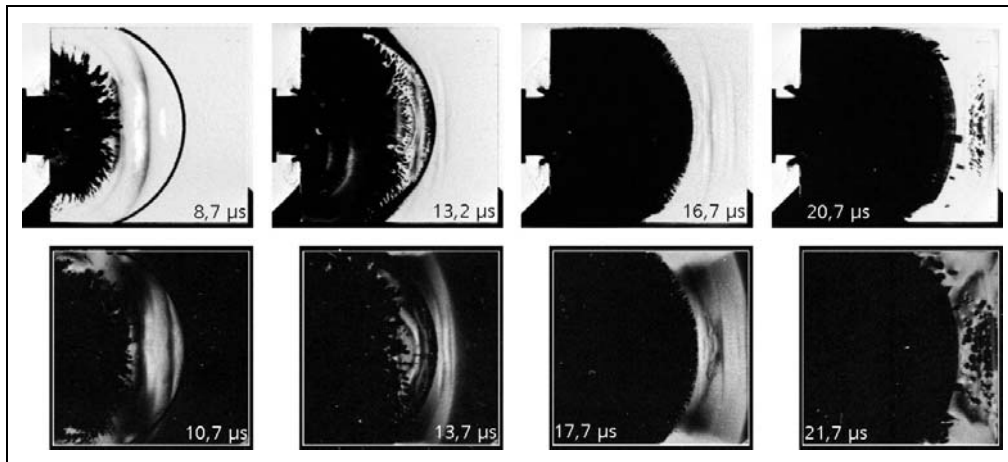


Figure 23. Selection of four shadowgraphs and corresponding crossed polarizers photographs; Starphire specimens with wave shaped interface; impact velocities 384/404 m/s.

As observed with the corrugated interface, cracks were initiated all along the wave shaped interface, which formed a dense crack front, propagating at a speed of 1514 m/s (see path-time history, figure 24).

The sets of high-speed photographs from the tests with modified interfaces have demonstrated that damage formation occurred in the second layer before the stress waves were reflected at the rear edge of the specimens. This means that the modified interfaces were less effective with respect to damage suppression or retardation compared to the laminates with straight interfaces. In contrast to the straight interfaces, the glass surfaces were not polished with the modified interfaces. Therefore, initial defects at the surfaces, due to machining of the specimens, could have caused stress concentrations and crack formation. The crack initiation at the tips of the saw tooth interface can possibly be attributed to this mechanism. However, the surfaces of the one thick specimen with straight interface, which was used as a reference, were not polished either and only little crack formation was observed in the second layer before reflection of the stress wave at the rear edge. Figure 25 shows a selection of four shadowgraphs from this baseline test.

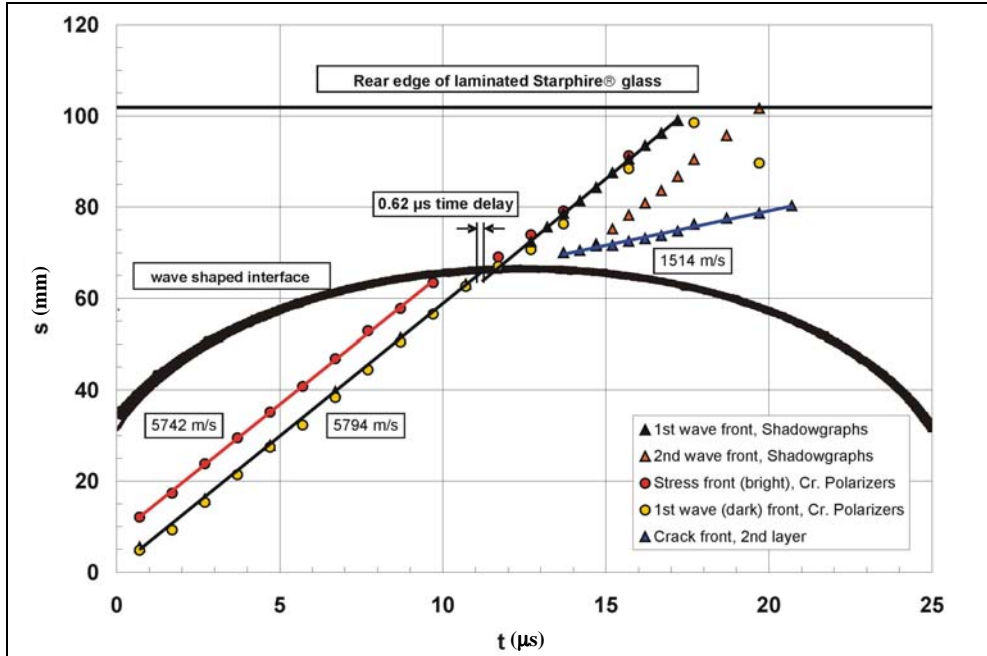


Figure 24. Path-time history of wave propagation in specimens with wave shaped interface.

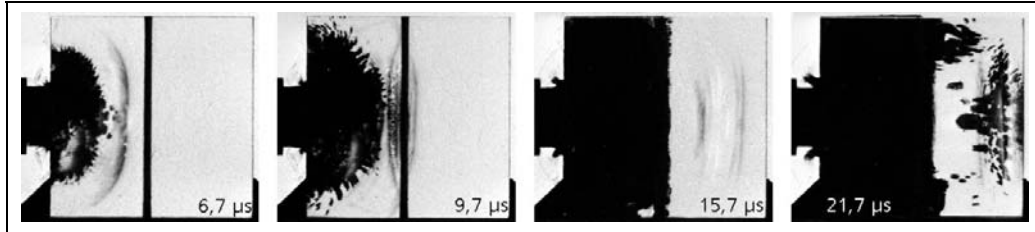


Figure 25. Selection of four shadowgraphs from baseline test with thick Starphire specimen with straight interface; impact velocity 404 m/s.

A specimen with two straight DF PU interfaces of 1.24 mm was impacted in such a way that the interfaces were parallel to the shot axis and the projectile only hit the intermediate glass layer (see figure 26). This impact configuration mimics the situation when a projectile hits one tile of a mosaic of ceramic tiles. The EOI technique allows for the observation of the wave and damage propagation in the adjacent tiles. Figure 27 shows the complete set of high-speed photographs, which were taken with the crossed polarizers set-up.

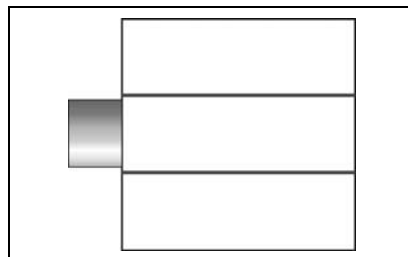


Figure 26. Schematic of EOI configuration to mimic impact on one tile of a ceramic mosaic.

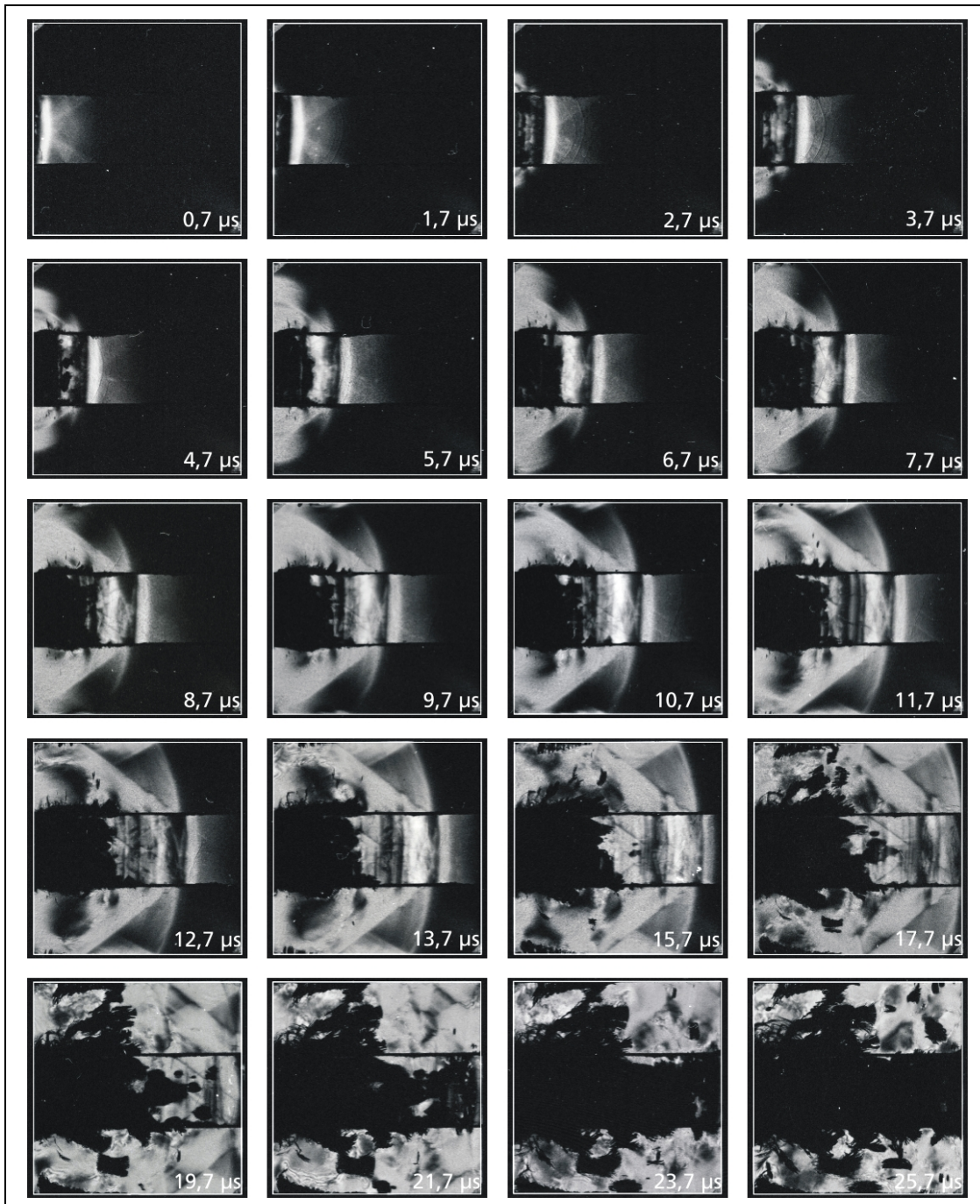


Figure 27. Complete set of high-speed photographs in crossed polarizers arrangement from EOI on intermediate glass layer, test no. 15726.

7. Results With AlON

Two pairs of tests were conducted with AlON in order to complement the earlier test series (5). The test parameters are listed in table 5.

Table 5. Tests with AlON.

Test No.	Projectile	Test Type	Imp. Velocity (m/s)	Opt. Set-up	Time intervals Picture No.: Δt (μs)
15281	Cylinder	Confinement	399	Shadowgraph	1–5: 1; 5–20: 0.5
15283	Cylinder	Confinement	394	Crossed polarizers	1–5: 1; 5–20: 0.5
15295	Sphere	Baseline	429	Shadowgraph	1–5: 1; 5–20: 0.5
15296	Sphere	Baseline	426	Crossed polarizers	1–5: 1; 5–20: 0.5

In the first pair of tests, the influence of a steel confinement was examined. Since the acoustic impedances of steel $T_{\text{Steel}} = 7.85 \cdot 10^3 \text{ kg/m}^3 \cdot 5100 \text{ m/s} = 40 \cdot 10^6 \text{ kg/m}^2 \text{s}$ and AlON $T_{\text{AlON}} = 3.69 \cdot 10^3 \text{ kg/m}^3 \cdot 10300 \text{ m/s} = 38 \cdot 10^6 \text{ kg/m}^2 \text{s}$ nearly match, a significant reduction of the amplitude of the reflected waves was expected, and therefore, a reduced influence of the reflected waves on the damage pattern. For this purpose, a target mount was designed, with an opening only for the projectile. Figure 28 shows a photograph of the target mount with an AlON specimen alone, and with the AlON specimen between crossed sheet polarizers. The surfaces of the square bar steels that were in contact with the AlON specimen were ground in order to improve the contact between the two materials. The photograph with specimen between crossed polarizers illustrates, that already relatively low stresses, caused by the mounting of the target, could be visualized.

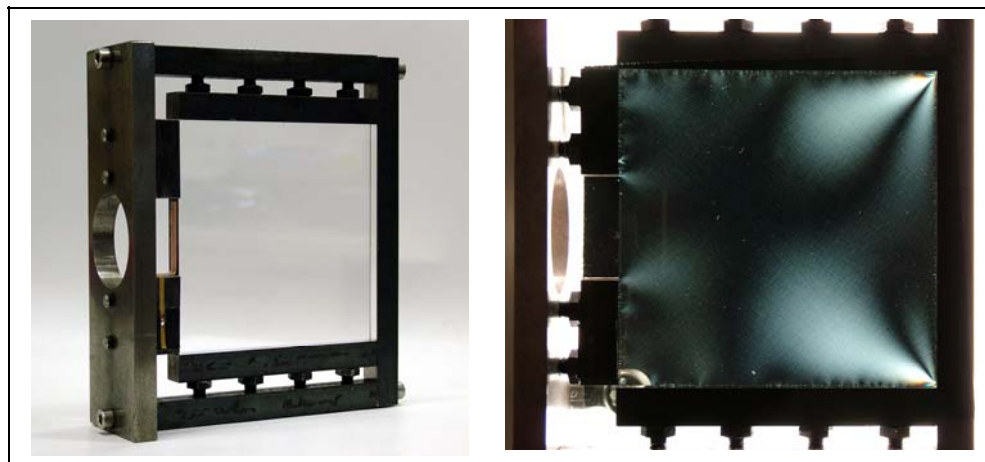


Figure 28. Photographs of target mount with AlON specimen (left) and mounted specimen between crossed (sheet) polarizers (right).

In the first test with confinement the high-speed camera was triggered too late, so that only a part of the sequence of photographs showed the damage development in the specimen. However, from the photographs of the test with crossed polarizers, not only the wave front could be recognized but also the development of the fracture front could be analyzed.

A selection of eight photographs from the test with steel confinement in the crossed polarizers configuration is presented in figure 29.

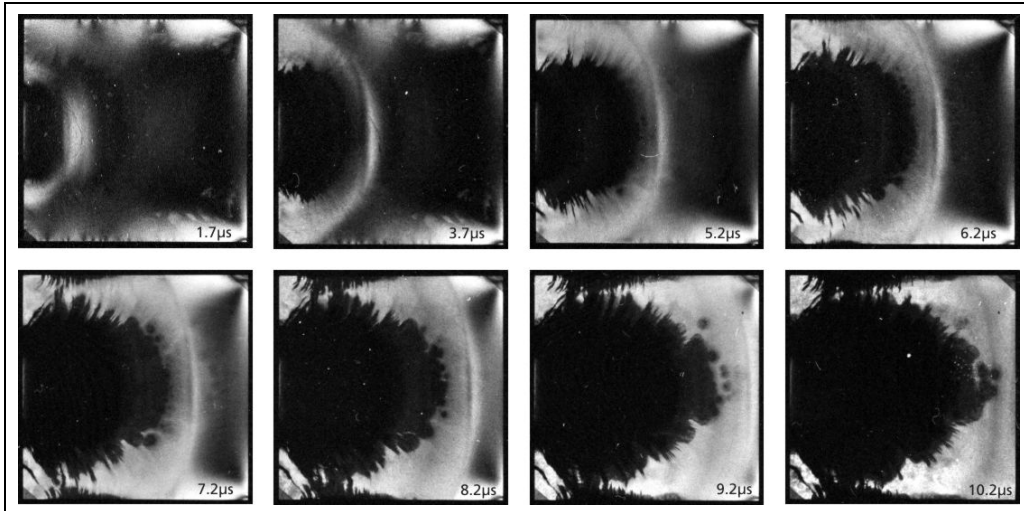


Figure 29. Selection of eight crossed polarizers photographs from test no. 15283 with steel confinement and impact velocity of 394 m/s.

The photographs show the nearly semicircular shaped stress wave (bright), followed by a coherent fracture front (dark), which is preceded by single crack centers. A clear boundary between the coherent fracture zone and the damage nucleation zone, where the crack centers appear, can not be recognized. The only significant difference in the total damage pattern compared to the tests without confinement is the growth of cracks from the upper and lower edge of the specimen. This crack growth could be due to the pre-stress on the specimen through the confinement. Figure 30 shows the path-time history of wave and damage propagation. A longitudinal wave velocity of 10,226 m/s has been determined, which is in good agreement with the value determined from the test with the spherical projectile (10,213 m/s). The best fit straight line through the nucleation sites of three leading edge crack centers yields a damage velocity of 9332 m/s. This is also very similar to the damage velocities obtained with unconfined specimens.

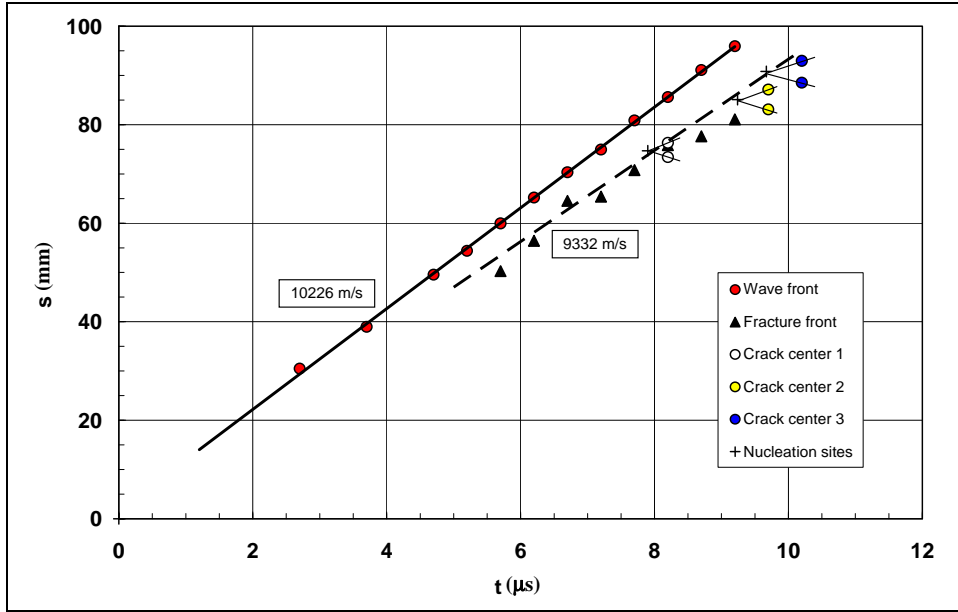


Figure 30. Path-time data of wave and fracture propagation in confined specimen, analysis of crossed polarizers photographs.

The damage pattern in AlON due to EOI of a spherical projectile at about 430 m/s is illustrated in figure 31, which shows a selection of four shadowgraphs and the corresponding crossed polarizers photographs. The sequence of photographs shows a fan-shaped fracture pattern, consisting of many single cracks, emanating from the center of impact. The semi-circular contour indicates that all cracks are growing at the same speed. The crossed polarizers photographs do not only show the longitudinal stress wave front, but also the transversal wave front. The path-time histories of the longitudinal and transversal waves and the crack front propagation are depicted in figure 32. The wave and crack velocities were determined by linear regression of the position-time data:

- Longitudinal wave speed (c_L) = 10,213 m/s;
- Transversal wave speed (c_T) = 5667 m/s; and
- Terminal crack velocity (v_{Cr}) = 4377 m/s.

8. Numerical Simulations

8.1 Introduction

The ansatz chosen here for a numerical modeling of ceramics is based on a discretization using finite elements.

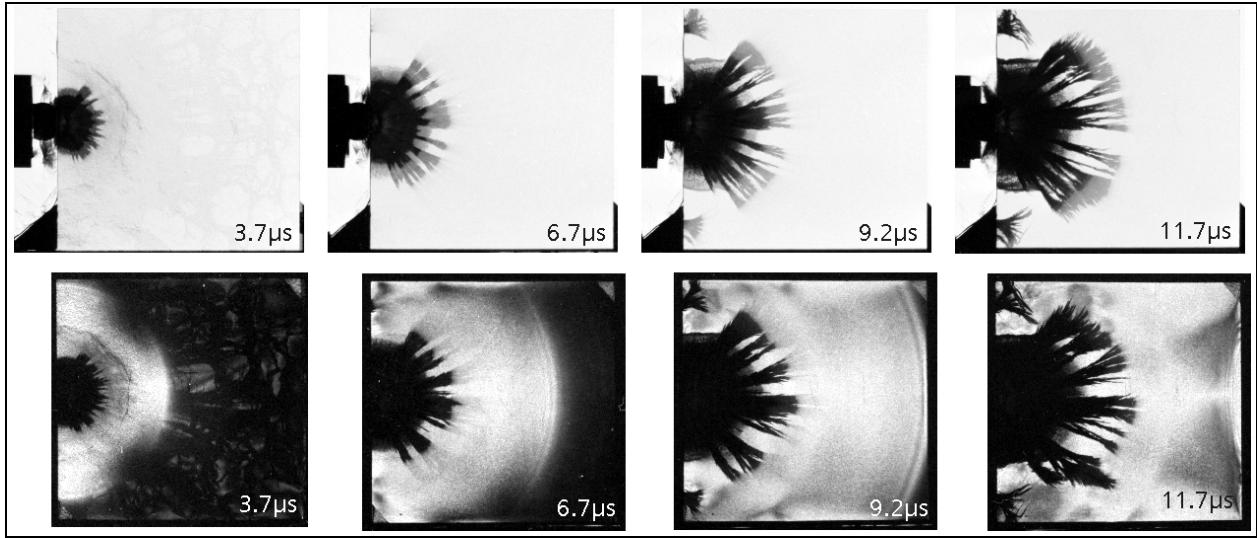


Figure 31. Selection of four shadowgraphs and corresponding crossed polarizers photographs from baseline tests with AlON; spherical projectile; test nos. 15295–96.

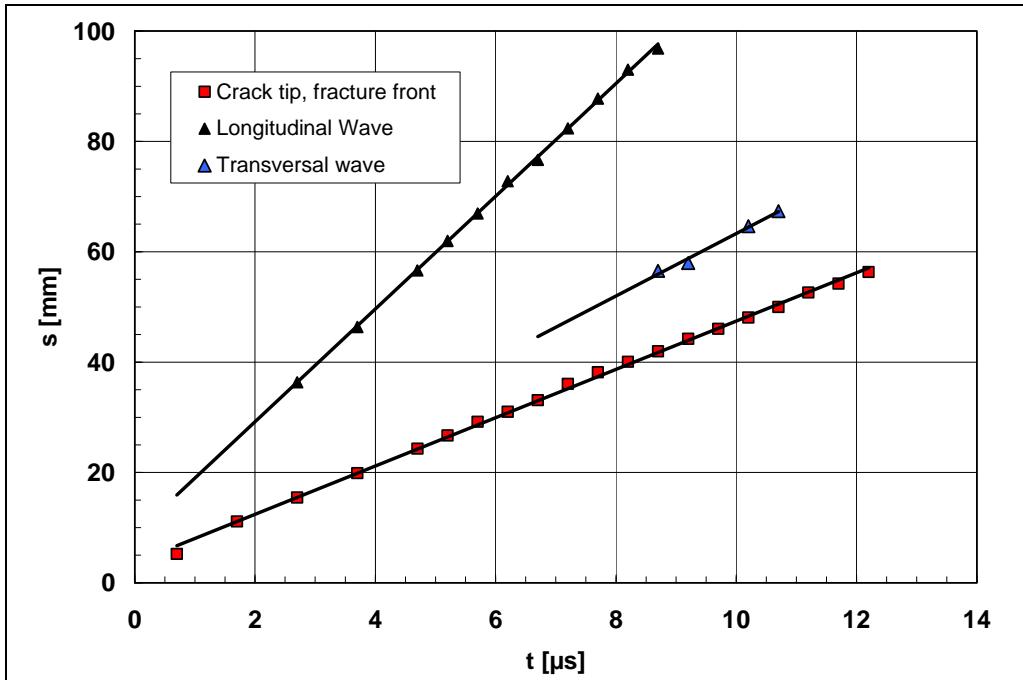


Figure 32. Path-time history of wave and crack propagation in AlON from baseline tests with spherical projectile; test nos. 15295–96.

In order to model the polyhedral microstructure of the ceramics under investigation as exactly as possible, we first implemented a code which is based on the theory of power diagrams (a generalization of voronoi diagrams) (6). With power diagrams, one can construct tessellations of 3-D space which correspond to a polyhedral cell complex. We implemented a subsequent optimization scheme (7–9), which changes the obtained cell structures according to the statistics

of grain sizes obtained from micrographs in two dimensions, the only available source for the actual grain structure of the materials on a micrometer scale. The generated power diagrams are polyhedral cell complexes in three dimensions and are optimized such that an arbitrary virtual cross section through the 3-D cell complex corresponds on average to the grains' circumference and size distribution. This procedure ensures that our obtained cell, respectively grain structure, is as close to the experimental evidence as possible.

After obtaining a 3-D grain structure that corresponds on average to what is observed in micrographs, we mesh these structures in three dimensions using tetrahedra in 3-D vs. triangles in two dimensions (2-D). For 2-D, we implemented a further refinement procedure for the mesh which removes very small edges and areas such that the mesh becomes treatable in a numerical FEM ansatz. The influence of this refinement on the grains' distribution functions is negligible.

After having meshed the cell structures, they are subject to FEM simulations using a commercial program package (LSDyna) which allows for a procedure that can treat grains as individually units, thus allowing an implementation of failure of grains (i.e., a separation of grains).

The next section illustrates our ansatz for generating and optimizing the grain structures as polyhedral cell complexes using power diagrams, along with the subsequent meshing and optimization procedure. Following that, the results of FEM simulations are displayed and discussed.

8.2 Generating Optimized Power Diagrams for FEM Analysis

Figure 33 displays our scheme for obtaining the cell area and perimeter distribution of scanned etched micrographs. The scanned micrographs are manually prepared by a vector graphics program with subsequent analysis using the KS 300 Imaging system by Carl Zeiss Vision GmbH. Figure 34 exhibits the only micrographs of ALON that were available for statistical sampling. Here, much larger samples would be needed in the future to obtain more reliable statistics.

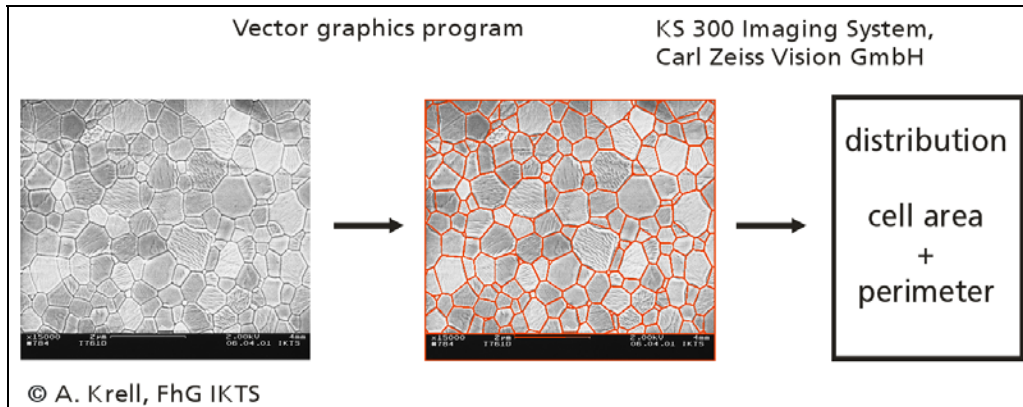


Figure 33. Scheme for obtaining the grains' distribution from etched micrographs. In this scheme, an Al_2O_3 micrograph is shown.

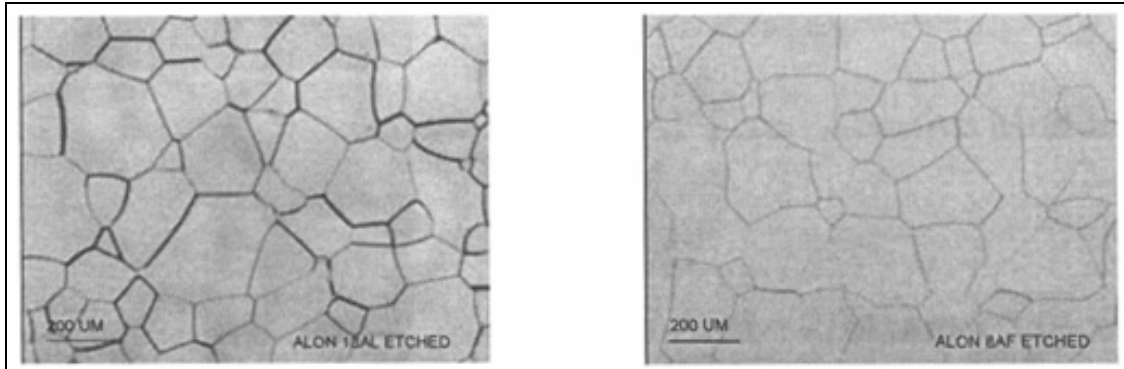


Figure 34. Available etched micrographs of aluminum oxynitride (ALON) (7). These micrographs were used to obtain optimized cell complex power diagrams in three dimensions.

Figure 35 explains our optimization scheme for the 3-D power diagram. Several hundreds of 2-D slices are taken for each orthogonal direction and taken into account for comparison with the experimental data. Figure 36 exhibits an example for a non-optimized power diagram, obtained as a cut through the 3-D cell complex. Figure 37 illustrates in a float diagram the algorithm of the optimization scheme whereas figure 38 displays the efficiency of our implemented optimization procedure. Figure 39 finally exhibits the results of the optimization of power diagrams. Due to insufficient statistical data on ALON available, we based our analysis on statistical data of Al_2O_3 . These data clearly outline the performance of our optimization scheme. As is evident from the figure, the optimized structure fits much better the underlying experimental data.

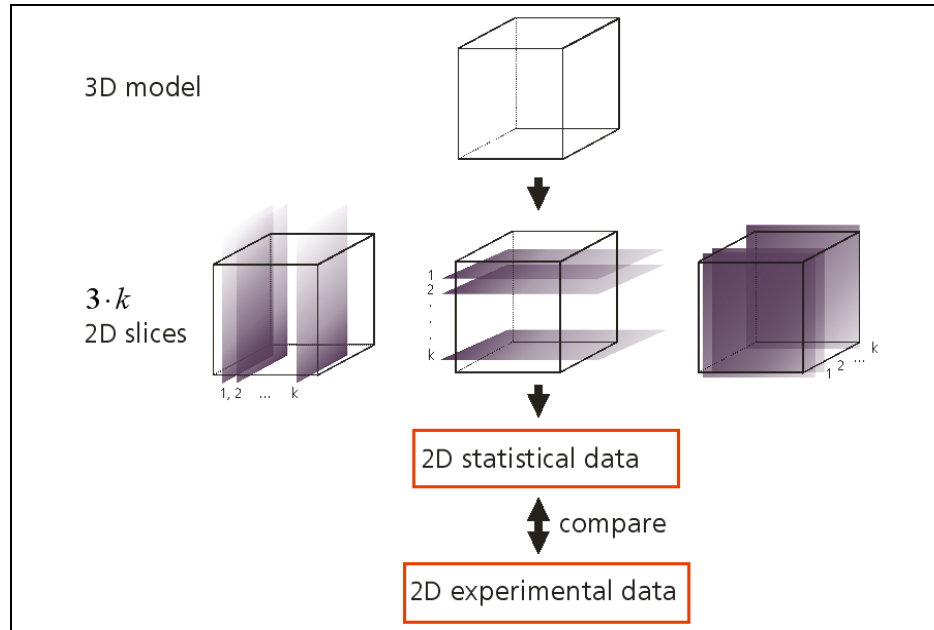


Figure 35. Optimization scheme for our 3-D model to obtain a polyhedral grain structure which corresponds to the (only) 2-D structural information available from etched micrographs.

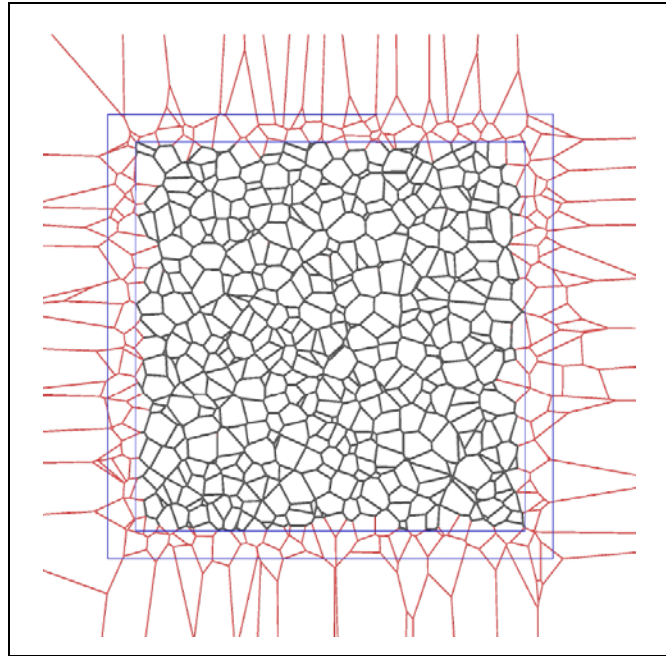


Figure 36. Example of a generated initial (not yet optimized) 2-D cut of our 3-D cell complex.

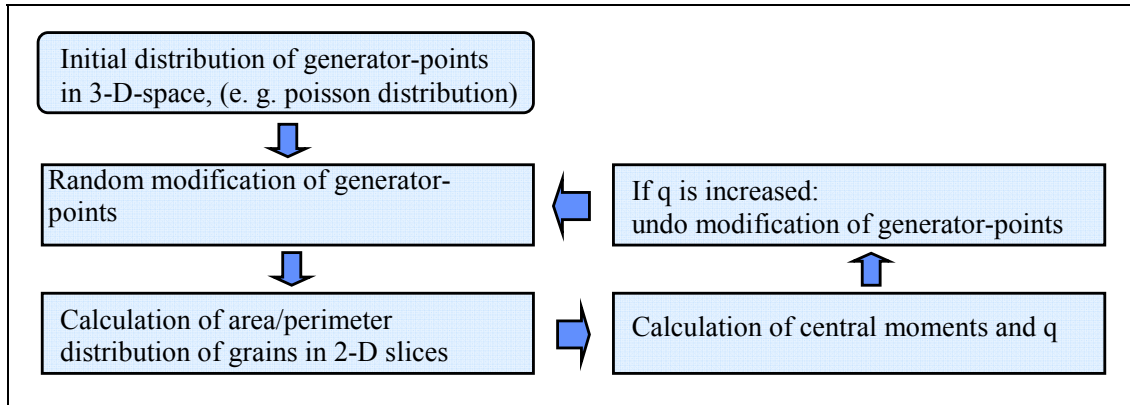


Figure 37. Optimization scheme for 3-D generated structures. We use the first three central moments for comparison of the generated structures with the distribution obtained from etched micrographs.

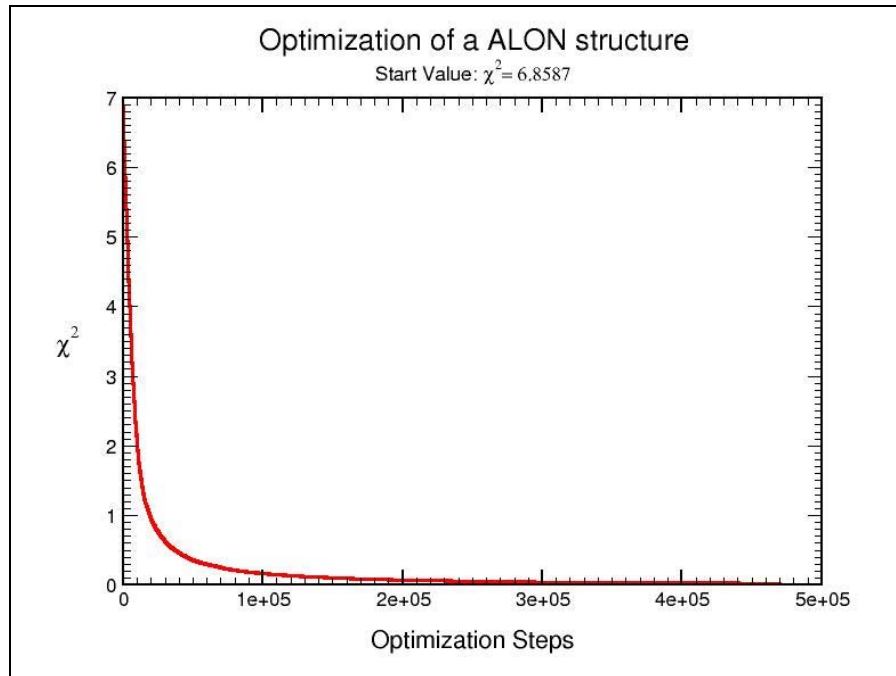


Figure 38. Efficiency of optimization procedure for ALON. After only 8 days of optimization, the coefficient χ^2 , which is a measure of the difference between the generated structure and the experimental data, is for all practical purposes very close to zero.

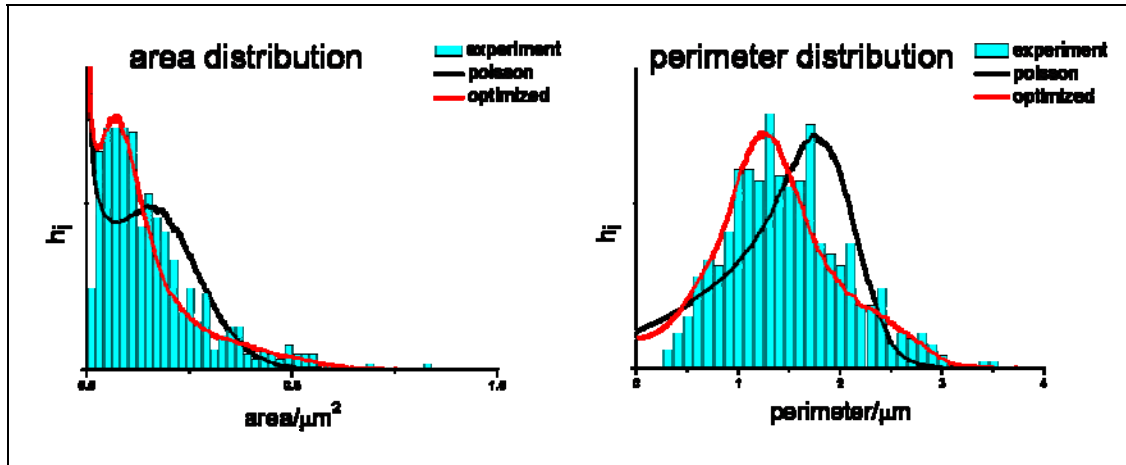


Figure 39. Demonstration of the result of the optimization procedure for the area and perimeter distribution for Al_2O_3 . The Poisson distribution is the one obtained from a non-optimized initial power diagram. The optimized grain structures fit much better the experimental data.

Figures 40 and 41 show an example of a 3-D generated voronoi structure in the shape of a cube and an SEM picture of a typical ceramics surface (in this case, Al_2O_3 , as no SEM pictures of ALON were available). Also by visual inspection it is evident that the 3-D grain structure of a ceramic specimen is very well modelled by our approach using power diagrams.

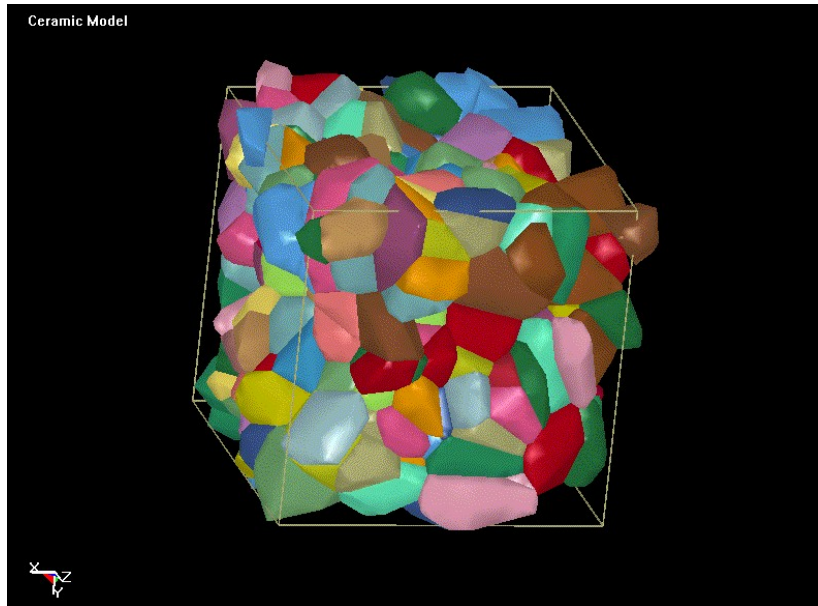


Figure 40. Generated and optimized 3-D grain structure of ALON. There is a total of 371 gr with a total of 130,000 elements in three dimensions. The grains are initially tied together by a contact force. Dimensions of the cube are arbitrary units as the size of the grains can be scaled to the desired size (in this case, $1 \times 1 \times 1$ mm).

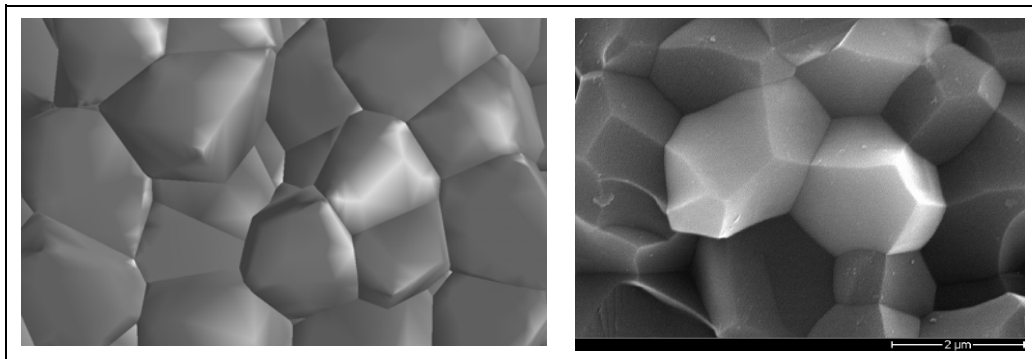


Figure 41. Direct comparison of a computer-generated granular surface (ALON) and a SEM picture of a typical ceramic grain structure, in this case Al_2O_3 .

Figures 42 and 43 illustrate a 2-D sample along with the meshing and the refinement procedure for the generated mesh which leads to a removal of short edges and areas.

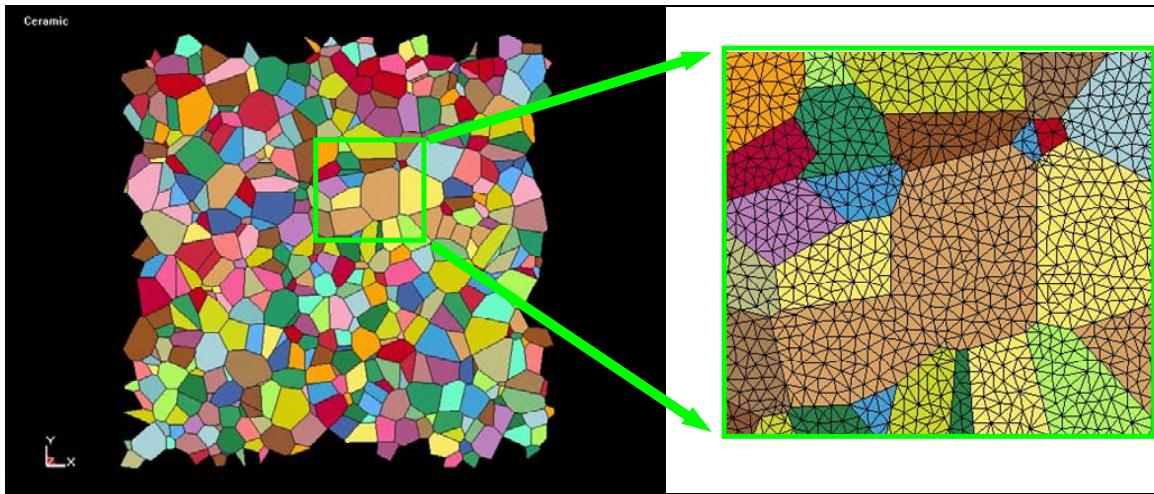


Figure 42. The 2-D cut through a 3-D cell structure and subsequent meshing of the grains. Note that there are no intermediate elements (such as shell or interface elements) used in between the various grains. There is an initial contact force applied to the knots of adjacent interfaces of grains.

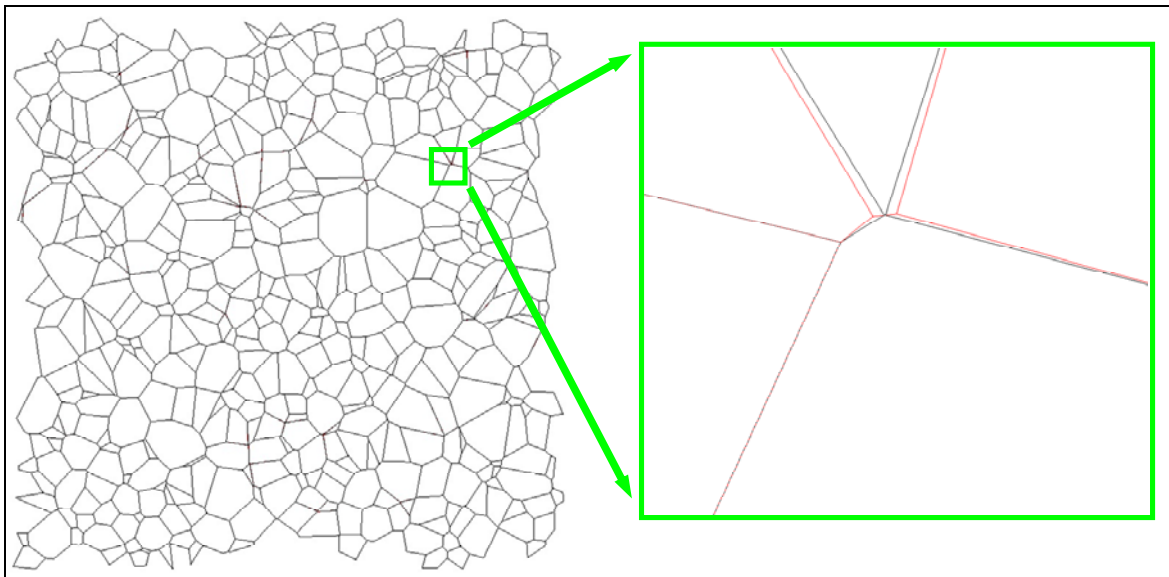


Figure 43. Illustration of a mesh optimization procedure in two dimensions which removes short edges (and areas) such that a larger time step in a subsequent FEM analysis can be used.

Finally, in figures 44 and 45, we display the various ways in which we are able to prepare samples from our power diagrams' raw data. Specimens with smooth edges are possible as well as structures in which the natural surface roughness due to the grains is kept.

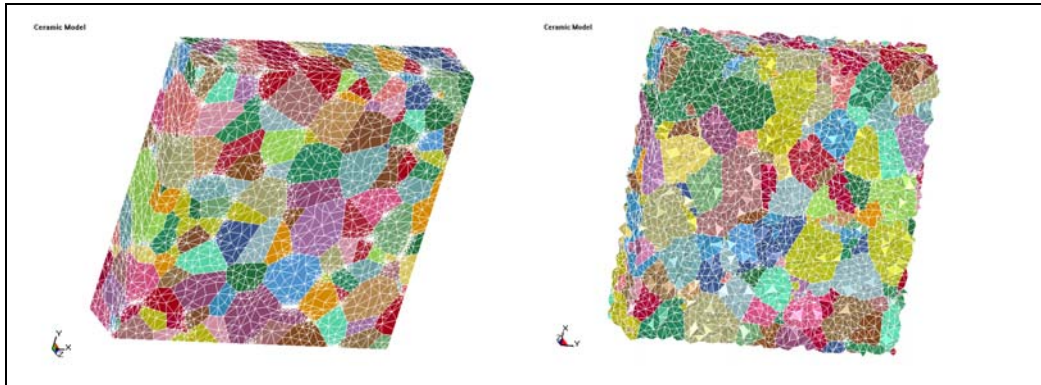


Figure 44. Illustration of different 3-D cuts through a generated power diagram. Structures with smooth edges or rough edges (leaving the surface grains unchanged) are possible.

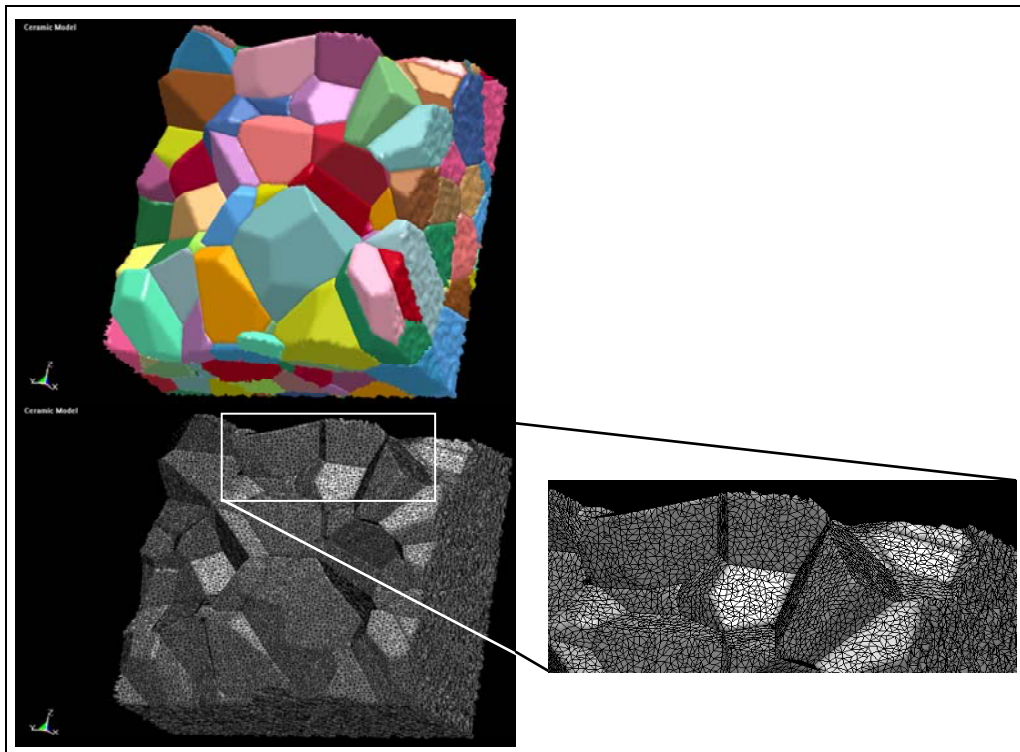


Figure 45. Another example of sample preparation from the raw data of the power diagram.
 Top: a view of the granular structure with different colors of grains for clarity.
 Bottom: the same structure but meshed with tetrahedral in three dimensions.
 Bottom right: another enlargement of a surface area exhibiting the meshed structure.

8.3 Model, Results, and Discussion

Our approach for modeling ALON is based on a FE discretization and takes into account the microstructure of densely sintered ceramics. The ceramics are modeled as a polyhedral cell complex such that the statistical properties agree well with experimental ceramic slices concerning the area distribution and the distribution of form-factors. The grains of these cell complexes were separated and meshed as individual objects. Finally these cells were tied again in the original configuration using a tiebreak contact implemented in the commercial FEM-code LS-DYNA. Crack opening is described by a cohesive softening law based on a fracture energy approach. This model was applied to an 8×8 -mm ALON-ceramics 2-D plain strain model hit by a steel-object at high velocity (430 m/s). A simple isotropic, linear elastic material model was used for the grains and for Young's modulus E . The maximum stress upon which intra-granular failure occurs and the fracture energy of the contacts were taken from macroscopic data. The results of the simulation are shown in figure 46.

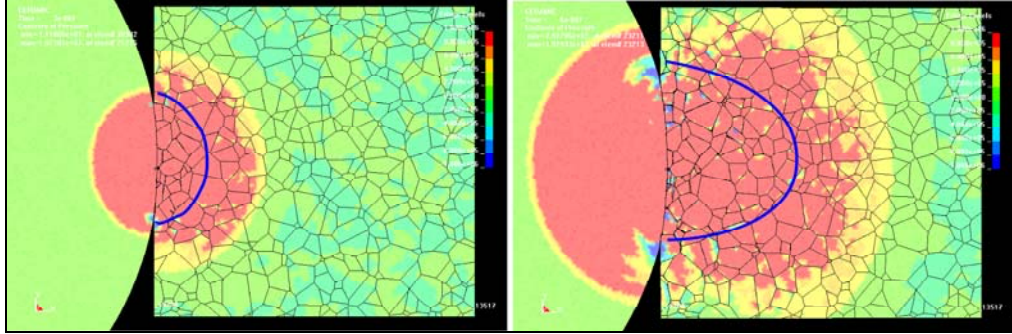


Figure 46. Left: ALON plate LS-DYNA model, 8×8 mm, $0.3 \mu\text{s}$ after being hit by a steel sphere at 430 m/s . Right: same model after $0.6 \mu\text{s}$; the colors mark the pressure level -1 GPa to $+1 \text{ GPa}$; the blue line marks a zone where most contacts have already failed.

The zone where fully developed cracks between individual grains can be observed is marked by a blue line. The growth rate of this zone is about half the velocity of the elastic wave speed, which compares well with experimental observations (figure 31). Under the assumption of a constant wave-velocity and symmetric behavior, one can qualitatively compare the model at $0.6 \mu\text{s}$ with the experiment at $6.7 \mu\text{s}$.

Note that our model does not include any arbitrary additional elements at the grain boundaries such as interface elements or shell elements, etc. In this case, one would always change the ratio of volume to surface within the grains and always overestimate the influence of the grain boundary. The grain boundaries are just areas of local atomic disorder of adjoining single crystals. The size of this area is negligibly small (a few Angstroms) compared to the typical size of a grain. Therefore we use an ansatz with contact forces at grain surfaces which initially glue the grains' knots at surfaces together and which does not use any additional and artificial

interface elements. As we have no experimental data for this crystal contact force, we used and tested different material models implemented in the commercial code LS-DYNA.

In a first attempt, we used material no. 96 in the commercial code LS-DYNA which allegedly is a model suited for the description of brittle damage. This model requires a number of material parameters as input, namely:

- Density
- Young's modulus E
- Poisson number ν
- tensile and shear stress limit
- fracture toughness
- compressive yield stress

We only had available E and the fracture toughness for AlON. The tensile and shear limit were taken as $8 \cdot 10^5$ Pa and $2 \cdot 10^5$ Pa, respectively, which is a ratio of four in reference to concrete.

The compressive yield stress was estimated as being close to that of Al_2O_3 . We tested this model in a total of 19 different parameter variations but in all variations it led to strong mesh distortion and subsequent termination of simulation due to numerical instabilities. Therefore, we finally used a simple piecewise elastic plastic material model for AlON provided by the LSDyna library using the material parameters of AlON (ρ , μ , E , and σ_f [10]) for the impacted specimen, and steel (from www.matweb.com) for the impactor. We then observe the correct wave velocity in the material ($\sim 10,040$ m/s) and a velocity of propagating cracks of ~ 4530 m/s which is in good agreement with the experiments (see figures 31 and 32).

Note that only by using this specific way of modeling, namely using tiebreak contacts between the grains, we are able to really model failure of the material and to avoid any artificial numerical behavior, as can be seen when modeling the target as a continuum without the microstructural details.

As an illustration of this, we simulated a full continuum model that does not contain any microstructural details using the commercial package Autodyn, and show that this model depends strongly on the chosen mesh resolution (see figure 47). In the left picture, the mesh resolution was 1 mm; in the right one it was 0.5 mm. The results of failure are completely different in these two pictures with otherwise identical simulation conditions. Also, the simulation using smooth particles does not lead to any improvement in this respect (see figure 48). Here, there are even more artifacts visible in respect to failed elements.

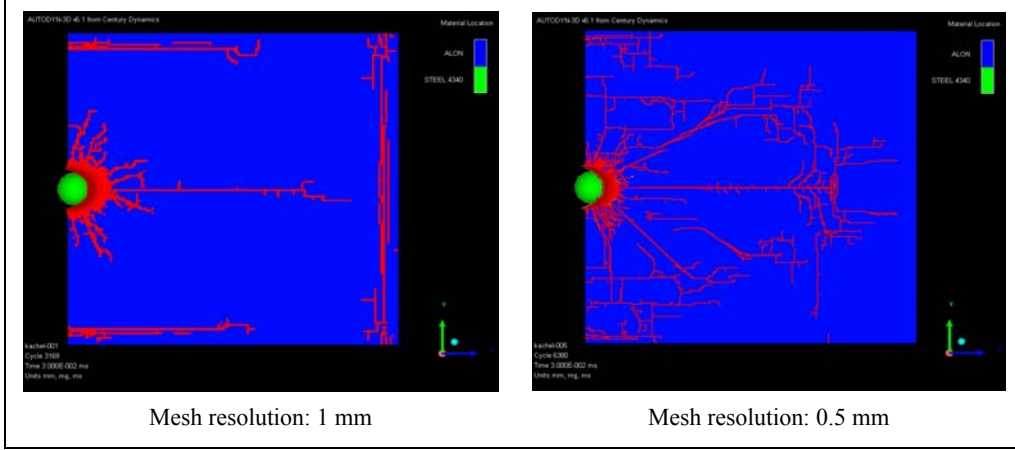


Figure 47. Insufficiency of generic FEM approaches. A steel impactor hits an AlON tile. Red: failed elements. Starting configuration of an EOI at $v_p = 50$ m/s.

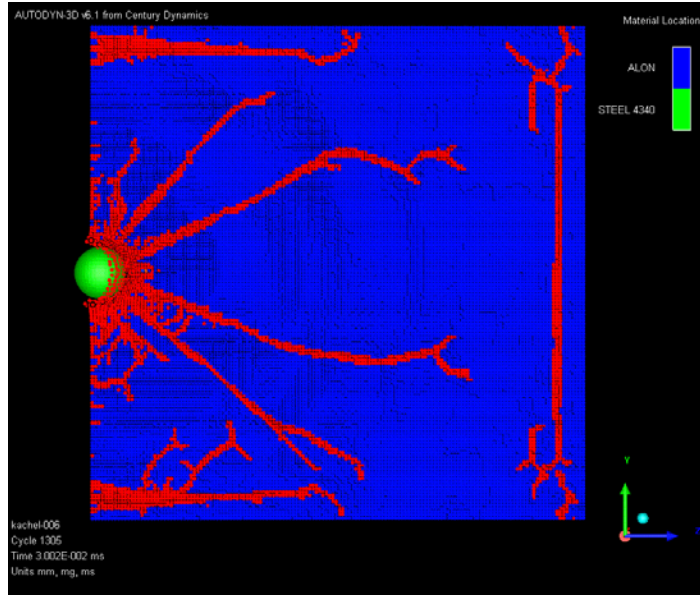


Figure 48. AlON modeled with SPH particles and a resolution of 1 mm. The result is different from the one in figure 47 (left), although all simulation conditions are the same.

Figures 49–51 show a series of snapshots from an impact simulation with a 2-D system of size 9×9 mm at $v_p = 430$ m/s. One can see nicely the onset of developing cracks in the material until complete failure with several chunks of failed material. Finally, in figure 52, the actual size limitations in the simulations are shown. Only a very small area of the ceramic tile can be simulated when the microstructure is taken into account explicitly.

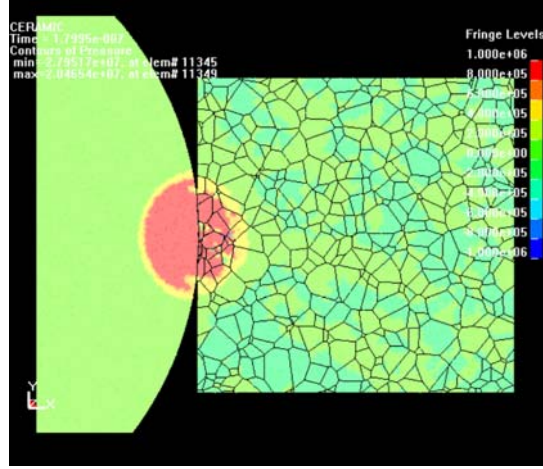


Figure 49. Impacted ALON at 450 m/s with a steel impactor, $1.8 \cdot 10^{-7}$ s after impact.

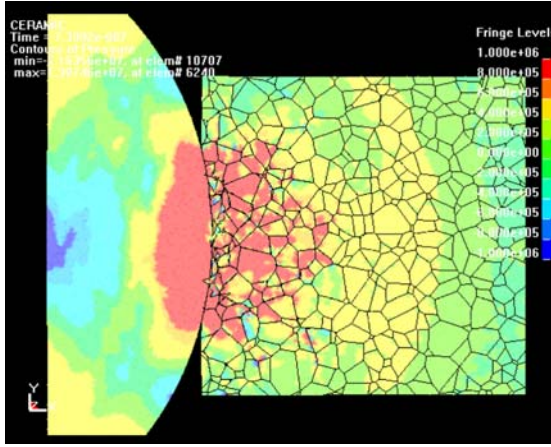


Figure 50. Impacted ALON at 450 m/s with a steel impactor, $7.4 \cdot 10^{-7}$ s after impact.
Comminution of the impact zone has already started.

8.4 Outlook (Numerical Simulation)

A fundamental problem which we are facing with our FEM approach is the fact that the algorithm which is implemented for the contact force is extremely expensive, thus rendering simulations of 3-D systems or *intra-grain* failure practically impossible. Even for 2-D systems, we are facing extremely small time steps and long simulation runs with more than 500,000 elements along with many numerical stability problems due to strong mesh distortions.

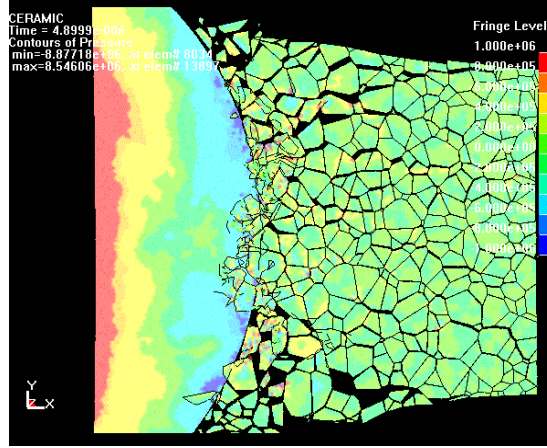


Figure 51. Impacted AlON at 450 m/s with a steel impactor, 4.9×10^{-6} s after impact.
Failure of the ceramic with different fracture pattern propagating through the ceramic tile.

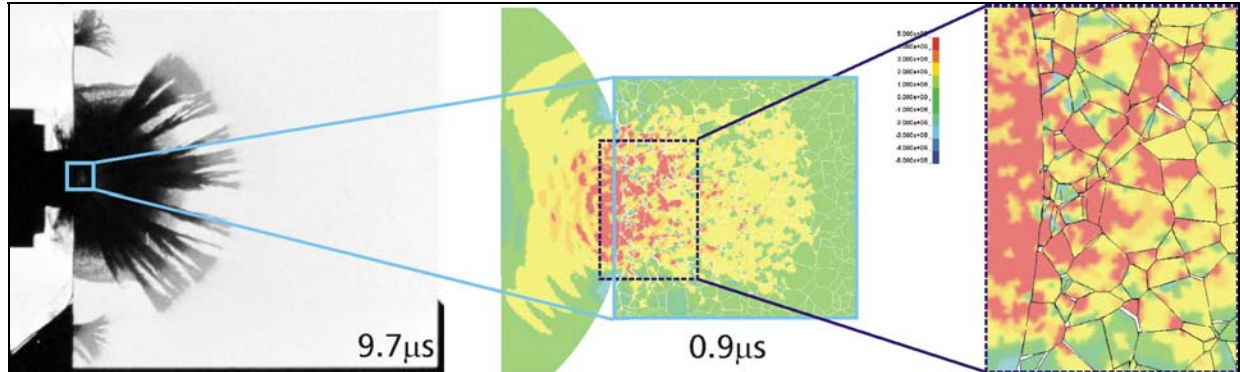


Figure 52. Snapshot of an impact experiment with a spherical steel impactor and the magnified simulated 2-D sections of the AlON ceramic tile which exhibit the damage zone after the impact. The simulation model is a 7.8×7.8 -mm 2 section of the original 100×100 -mm 2 tile. Using an elastic plastic material model, the wave velocities in the experiment and in the simulations are the same. The simulation snapshot is taken after the shock wave has crossed about 70% of the simulated part of the tile. Displayed minimum and maximum pressure is ± 1 GPa.

What is necessary in these endeavors is the development of an apt and more efficient code structure, optimized for simulating failure in a mesh without using additional interface elements. Also, more etched 2-D viewgraphs displaying the granular structure of AlON would be very helpful for an enhanced optimization of the power diagrams. A different method for simulating fracture and failure in ceramics, developed by Steinhauser et al. (11–13), based on overlapping particles interacting via potentials, shows very promising results for further investigations along this direction. However, with the limitations of time and resources within this project, further development of this method was not feasible.

9. Conclusion

The EOI test method was applied in order to visualize wave and damage propagation in materials for transparent armor. The influence of bonding layer thickness on damage evolution in Starphire glass laminates was examined. The high resolution of the high-speed photographs allowed for the determination of the stress wave time delay during the transition through the bonding layers. It is expected that the capabilities of the experimental method help with the development of damage models and that the combination of experimental and computational modelling results can eventually guide materials and laminates design.

10. References

1. Straßburger, E. *High-Speed Photographic Study of Wave Propagation and Impact Damage in Transparent Laminates*; 1st Interim Report, Contract No. N62558-05-P-0303; EMI-Report E 16/06; Efringen-Kirchen, Germany, March 2006.
2. Straßburger, E.; Senf, H. *Experimental Investigations of Wave and Fracture Phenomena in Impacted Ceramics and Glasses*; Final Report, Contract No. DAJA 45-90-C-0053; ARL-CR-214; U.S. Army Research Laboratory: Aberdeen Proving Ground, MD, February 1995.
3. Straßburger, E.; Steinhauser, M. *High-Speed Photographic Study of Wave Propagation and Impact Damage in Transparent Laminates*; 2nd Interim Report, Contract No. N62558-05-P-0303; EMI-Report E 24/06; Efringen-Kirchen, Germany, July 2006.
4. Gupta, Y. M. High Strain-Rate Shear Deformation of a Polyurethane Elastomer Subjected to Impact Loading. *Polymer Engineering and Science* **1984**, 24, (11).
5. Straßburger, E. *High-Speed Photographic Study of Wave Propagation and Impact Damage in Transparent Aluminum Oxynitride (AlON)*; Final Report, Contract No. N62558-04-P-6031, EMI-Report E 08/06, re-published as ARL-CR-579; U.S. Army Research Laboratory: Aberdeen Proving Ground, MD, 2006.
6. Aurenhammer, F. Power-Diagrams: Properties, Algorithms and Applications. SIAM. *Journal on Computing* **1987**, 16, 78–96.
7. Kühn, M. Optimierung von Power-Diagrammen zur Modellierung keramischer Mikrostrukturen, Diploma Thesis Fern-Universität in Hagen, EMI-Report 15/05, Oktober 2005.
8. Steinhauser, M.; Kühn, M. Numerical Simulation of fracture and Failure in Brittle Solids. *Presented at the Annual Meeting of the Gesellschaft für Angewandte Mathematik und Mechanik e.V. (GAMM)*, Technische Universität Berlin, March 2006.
9. Kühn, M.; Steinhauser, M. Modelling of Microstructures in Ceramics to Simulate Crack Growth. *Presented at the Annual Meeting of the Gesellschaft für Angewandte Mathematik und Mechanik e.V. (GAMM)*, Technische Universität Berlin, March 2006.
10. Hartnett, T. M.; Warner, C. T.; Fisher, D.; Sunne, W. Characterization of ALON Optical Ceramic. *Presented at the 107th Annual Meeting of the American Ceramic Society*, Baltimore, MD, April 2005.

11. Steinhauser, M. O.; Grass, K.; Thoma, K.; Blumen, A. Impact Dynamics and Failure of Brittle Solid States by Means of Nonequilibrium Molecular Dynamics Simulations. *Europhys. Lett.* **2006**, 72 (1).
12. Steinhauser, M. O.; Kühn, M. Modeling of Shock-Wave Failure in Brittle Materials, In: *Gumbsch, Peter (Editor): MMM Multiscale Materials Modelling (3rd Int. Conference on Multiscale Materials Modeling (MMM), Freiburg, Germany, 18.-22. 09. 2006)*. Proceedings; Fraunhofer IRB Verlag, 2006, pp 380–382.
13. Steinhauser, M. O.; Kühn, M. Numerical Simulation of Fracture and Failure Dynamics in Brittle Solids. In: *Khan, Akhtar, S., Kohei, Amir, R. (Eds.): Anisotropy, Texture, Dislocations, Multiscale Modeling in Finite Plasticity and Viscoplasticity and Metal Forming: (The 12th Int. Symposium on Plasticity and Its Current Applications, Halifax, Nova Scotia, Canada, 17.-22.07.2006)*. Proceedings; Neat Press, 2006, pp 634–636 (*Plasticity 2006*).

INTENTIONALLY LEFT BLANK.

**Appendix. Complete Sets of High-Speed Photographs From
Edge-on-Impact (EOI) Tests**

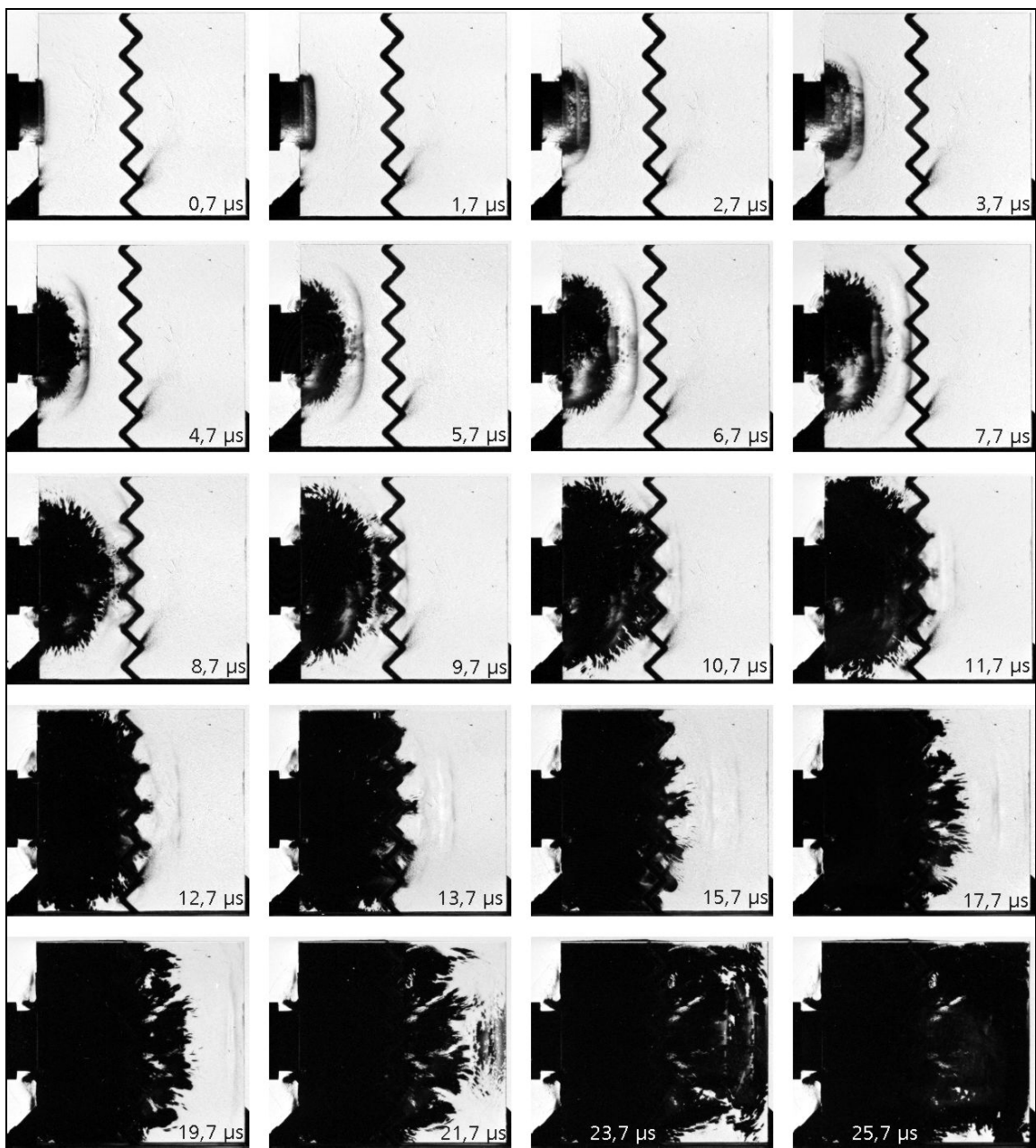


Figure A-1. Complete set of high-speed photographs from EOI test of laminated Starphire specimen with saw tooth interface, shadowgraph configuration; test no. 15724.

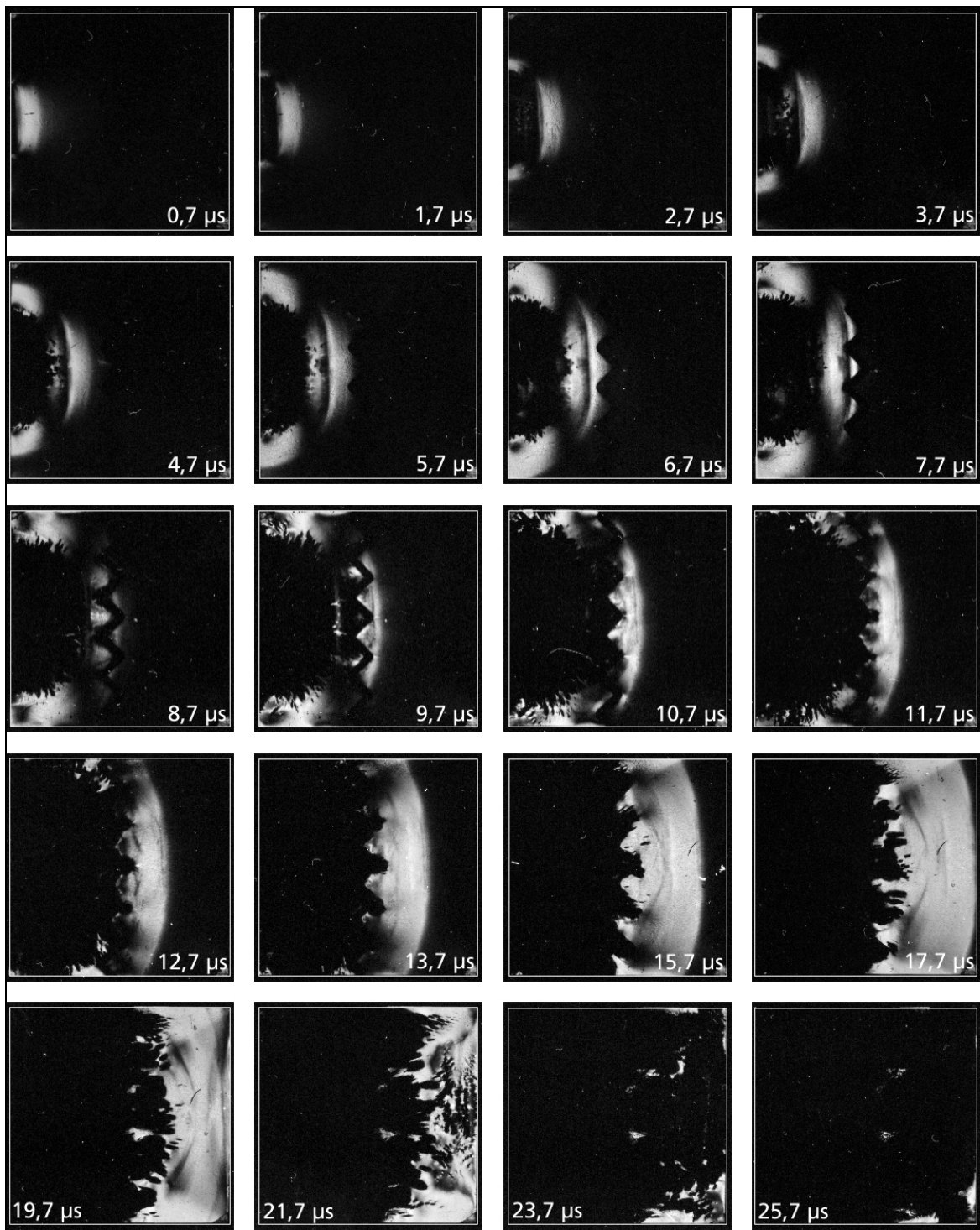


Figure A-2. Complete set of high-speed photographs from EOI test of laminated Starphire specimen with saw tooth interface, crossed polarizers configuration; test no. 15725.

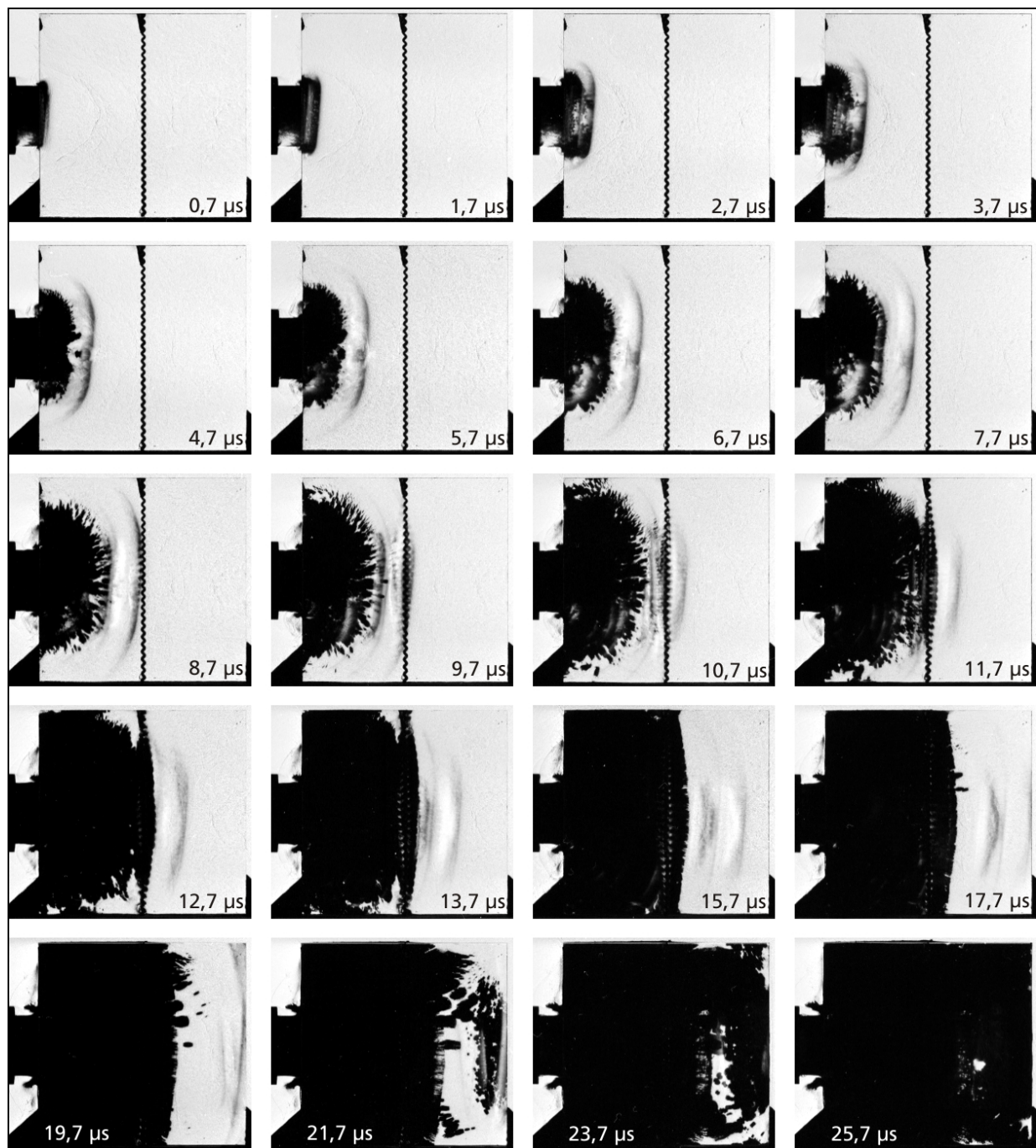


Figure A-3. Complete set of high-speed photographs from EOI test of laminated Starphire specimen with corrugated interface, shadowgraph configuration; test no. 15727.

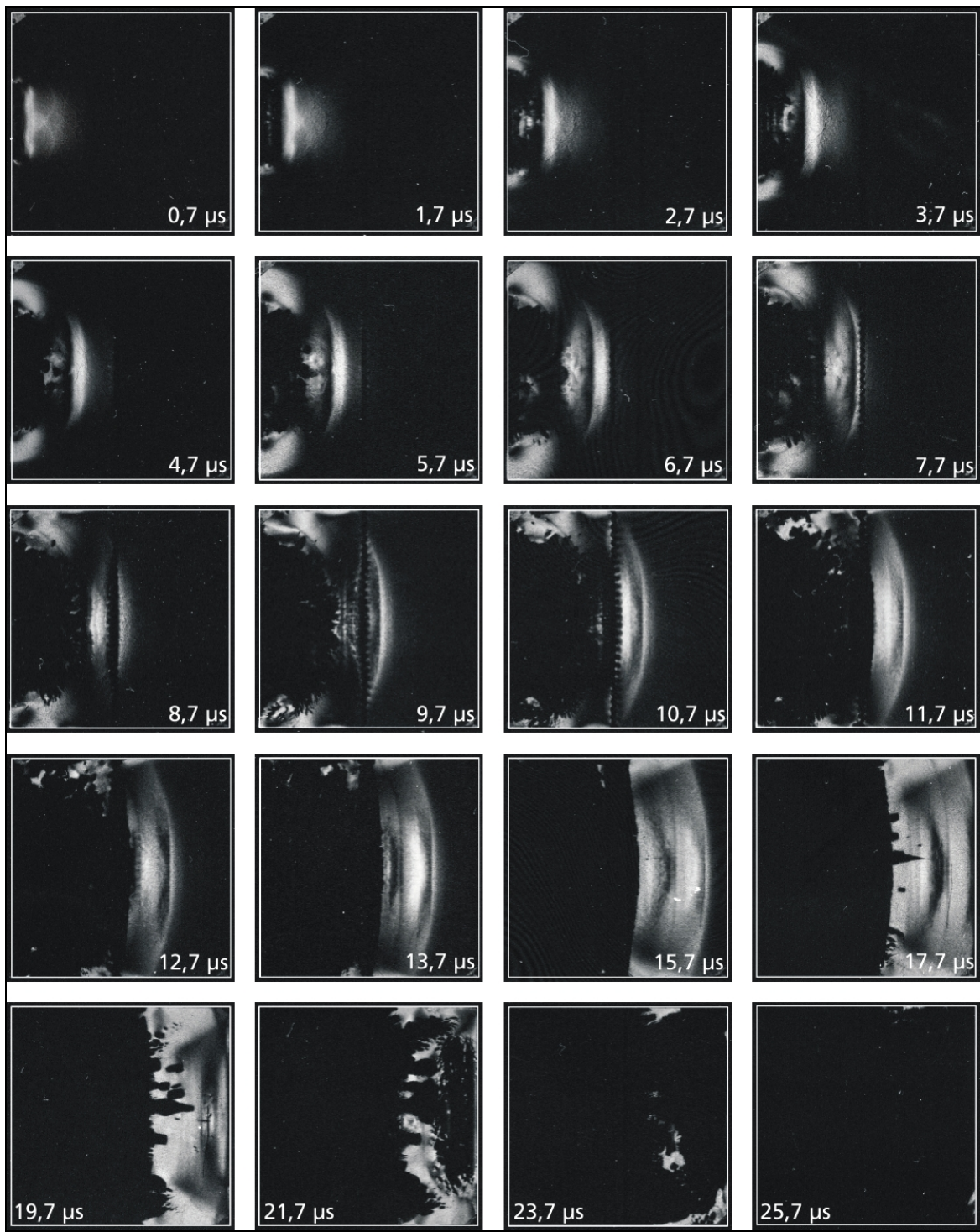


Figure A-4. Complete set of high-speed photographs from EOI test of laminated Starphire specimen with corrugated interface, crossed polarizers configuration; test no. 15728.

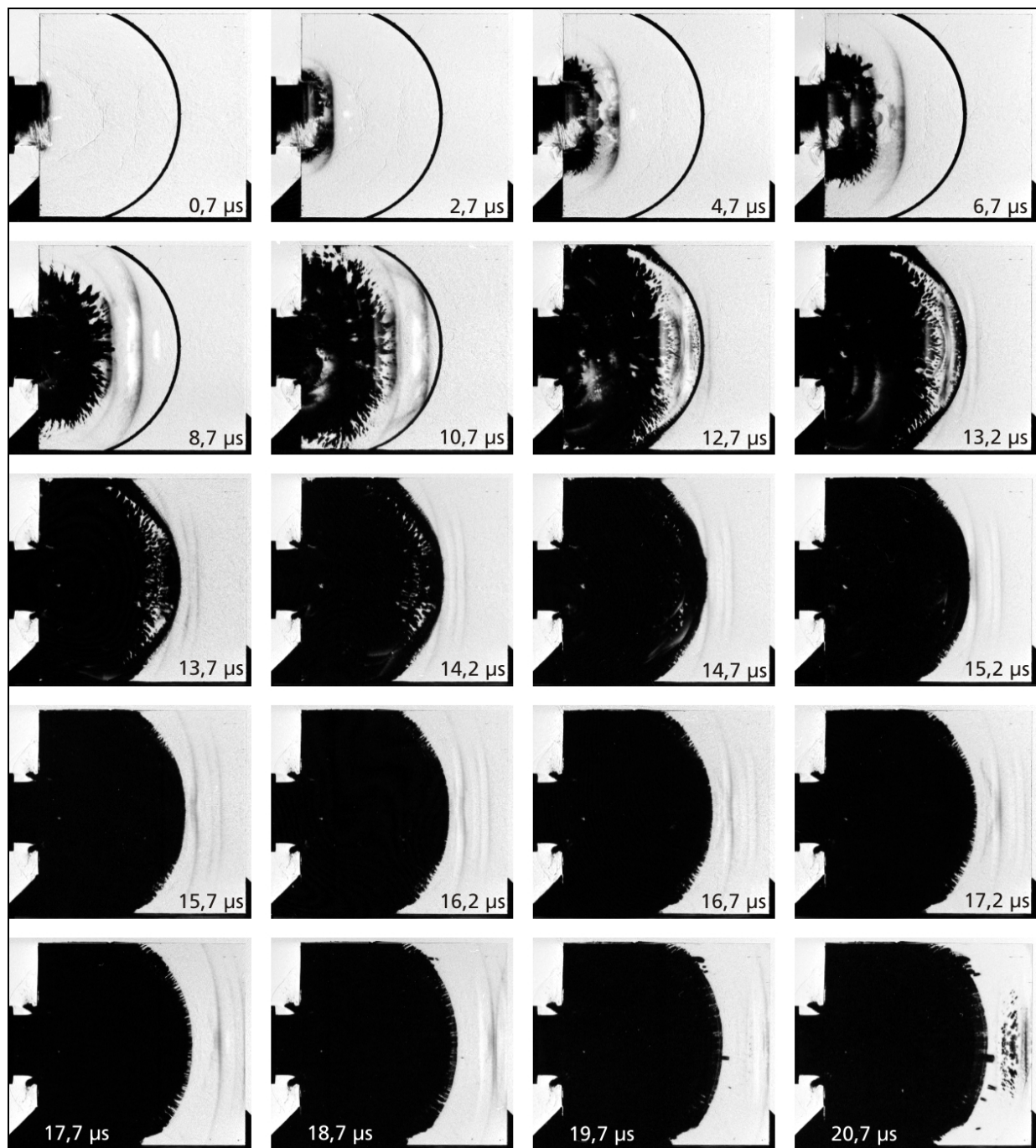


Figure A-5. Complete set of high-speed photographs from EOI test of laminated Starphire specimen with wave shaped interface, shadowgraph configuration; test no. 15731.

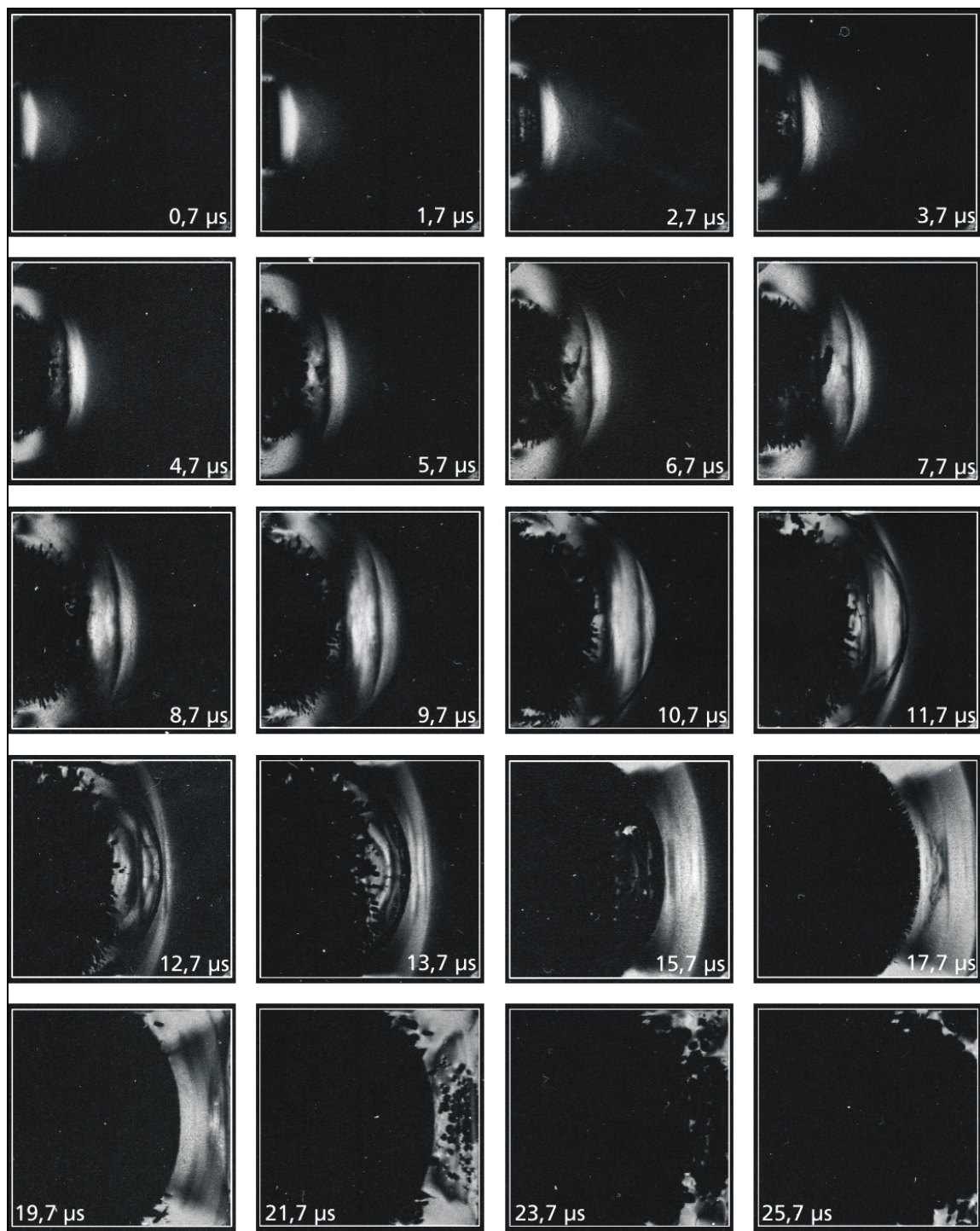


Figure A-6. Complete set of high-speed photographs from EOI test of laminated Starphire specimen with wave shaped interface, crossed polarizers configuration; test no. 15730.

NO. OF
COPIES ORGANIZATION

1 DEFENSE TECHNICAL
(PDF INFORMATION CTR
ONLY) DTIC OCA
8725 JOHN J KINGMAN RD
STE 0944
FORT BELVOIR VA 22060-6218

1 US ARMY RSRCH DEV &
ENGRG CMD
SYSTEMS OF SYSTEMS
INTEGRATION
AMSRD SS T
6000 6TH ST STE 100
FORT BELVOIR VA 22060-5608

1 DIRECTOR
US ARMY RESEARCH LAB
IMNE ALC IMS
2800 POWDER MILL RD
ADELPHI MD 20783-1197

1 DIRECTOR
US ARMY RESEARCH LAB
AMSRD ARL CI OK TL
2800 POWDER MILL RD
ADELPHI MD 20783-1197

1 DIRECTOR
US ARMY RESEARCH LAB
AMSRD ARL CI OK T
2800 POWDER MILL RD
ADELPHI MD 20783-1197

ABERDEEN PROVING GROUND

1 DIR USARL
AMSRD ARL CI OK TP (BLDG 4600)

<u>NO. OF COPIES</u>	<u>ORGANIZATION</u>	<u>NO. OF COPIES</u>	<u>ORGANIZATION</u>
1	ODUSD (SANDT) WS L SLOTER ROSSLYN PLAZA N STE 9030 1777 N KENT ST ARLINGTON VA 22209-2210	1	NAVAL SURFACE WARFARE CTR DAHlgren DIV CODE G06 DAHlgren VA 22448
1	COMMANDER US ARMY MATERIEL CMD AMXMI INT 9301 CHAPEK RD FT BELVOIR VA 22060-5527	1	USA SBCCOM PM SOLDIER SPT AMSSB PM RSS A J CONNORS KANSAS ST NATICK MA 01760-5057
1	OFC OF NAVAL RSRCH J CHRISTODOULOU ONR CODE 332 800 N QUINCY ST ARLINGTON VA 22217-5600	3	AIR FORCE ARMAMENT LAB AFATL DLJW W COOK D BELK J FOSTER EGLIN AFB FL 32542
1	PEO GCS SFAE GCS BCT/MS 325 M RYZYI 6501 ELEVEN MILE RD WARREN MI 48397-5000	1	DPTY ASSIST SCY FOR R&T SARD TT ASA (ACT) J PARMENTOLA THE PENTAGON RM 3E479 WASHINGTON DC 20310-0103
1	ABRAMS TESTING SFAE GCSS W AB QT J MORAN 6501 ELEVEN MILE RD WARREN MI 48397-5000	2	DARPA W COBLENZ L CHRISTODOULOU 3701 N FAIRFAX DR ARLINGTON VA 22203-1714
1	COMMANDER WATERVLIET ARSENAL SMCWV QAE Q B VANINA BLDG 44 WATERVLIET NY 12189-4050	1	US ARMY TACOM ARDEC AMSRD AAR AEW W E BAKER BLDG 3022 PICATINNY ARSENAL NJ 07806-5000
2	SFSJM CDL AMMUNITION TEAM R CRAWFORD W HARRIS 1 ROCK ISLAND ARSENAL ROCK ISLAND IL 61299-6000	11	US ARMY TARDEC AMSTRA TR R MS 263 K BISHNOI D TEMPLETON (10 CPS) WARREN MI 48397-5000
2	COMMANDER US ARMY AMCOM AVIATION APPLIED TECH DIR J SCHUCK FT EUSTIS VA 23604-5577	1	COMMANDER US ARMY RSRCH OFC A RAJENDRAN PO BOX 12211 RSRCH TRIANGLE PARK NC 27709-2211

<u>NO. OF COPIES</u>	<u>ORGANIZATION</u>	<u>NO. OF COPIES</u>	<u>ORGANIZATION</u>
2	CALTECH G RAVICHANDRAN T AHRENS MS 252 21 1201 E CALIFORNIA BLVD PASADENA CA 91125	1	COORS CERAMIC CO T RILEY 600 NINTH ST GOLDEN CO 80401
5	SOUTHWEST RSRCH INST C ANDERSON K DANNEMANN T HOLMQUIST G JOHNSON J WALKER PO DRAWER 28510 SAN ANTONIO TX 78284	1	UNIV OF DAYTON RSRCH INST N BRAR 300 COLLEGE PARK MS SPC 1911 DAYTON OH 45469-0168
2	UNIV OF DELAWARE DEPT OF MECH ENGR J GILLESPIE NEWARK DE 19716	2	COMMANDER US ARMY TACOM AMSTA TR S T FURMANIAK L PROKURAT FRANKS WARREN MI 48397-5000
3	SRI INTERNATIONAL D CURRAN D SHOCKEY R KLOOP 333 RAVENSWOOD AVE MENLO PARK CA 94025	1	PROJECT MANAGER ABRAMS TANK SYSTEM J ROWE WARREN MI 48397-5000
1	APPLIED RSRCH ASSOCIATES D GRADY 4300 SAN MATEO BLVD NE STE A220 ALBUQUERQUE NM 87110	3	COMMANDER US ARMY RSRCH OFC B LAMATINA D STEPP W MULLINS PO BOX 12211 RSRCH TRIANGLE PARK NC 27709-2211
1	INTERNATIONAL RSRCH ASSOCIATES INC D ORPHAL 4450 BLACK AVE PLEASANTON CA 94566	1	NAVAL SURFACE WARFARE CTR CARDEROCK DIVISION R PETERSON CODE 28 9500 MACARTHUR BLVD WEST BETHESDA MD 20817-5700
1	BOB SKAGGS CONSULTANT S R SKAGGS 7 CAMINO DE LOS GARDUNOS SANTA FE NM 87506	4	LAWRENCE LIVERMORE NATL LAB R GOGOLEWSKI L290 R LANDINGHAM L369 J E REAUGH L282 S DETERESA PO BOX 808 LIVERMORE CA 94550
2	WASHINGTON ST UNIV INST OF SHOCK PHYSICS Y GUPTA J ASAY PULLMAN WA 99164-2814		

<u>NO. OF COPIES</u>	<u>ORGANIZATION</u>	<u>NO. OF COPIES</u>	<u>ORGANIZATION</u>
6	SANDIA NATL LAB J ASAY MS 0548 R BRANNON MS 0820 L CHHABILDAS MS 0821 D CRAWFORD ORG 0821 M KIPP MS 0820 T VOLGER PO BOX 5800 ALBUQUERQUE NM 87185-0820	1	JET PROPULSION LAB IMPACT PHYSICS GROUP M ADAMS 4800 OAK GROVE DR PASADENA CA 91109-8099
3	RUTGERS THE STATE UNIV OF NEW JERSEY DEPT OF CRMCS & MATLS ENGRNG R HABER 607 TAYLOR RD PISCATAWAY NJ 08854	3	OGARA HESS & EISENHARDT G ALLEN D MALONE T RUSSELL 9113 LE SAINT DR FAIRFIELD OH 45014
2	THE UNIVERSITY OF TEXAS AT AUSTIN S BLESS IAT 3925 W BRAKER LN STE 400 AUSTIN TX 78759-5316	2	CERADYNE INC M NORMANDIA 3169 REDHILL AVE COSTA MESA CA 96626
3	SOUTHWEST RSRCH INST C ANDERSON J RIEGEL J WALKER 6220 CULEBRA RD SAN ANTONIO TX 78238	3	JOHNS HOPKINS UNIV DEPT OF MECH ENGRNG K T RAMESH 3400 CHARLES ST BALTIMORE MD 21218
1	CERCOM R PALICKA 991 PARK CENTER DR VISTA CA 92083	2	SIMULA INC V HORVATICH V KELSEY 10016 51ST ST PHOENIX AZ 85044
6	GDLS W BURKE MZ436 21 24 G CAMPBELL MZ436 30 44 D DEBUSSCHER MZ436 20 29 J ERIDON MZ436 21 24 W HERMAN MZ435 01 24 S PENTESCU MZ436 21 24 38500 MOUND RD STERLING HTS MI 48310-3200	3	UNITED DEFNS LIMITED PATERNERS GROUND SYS DIV E BRADY R JENKINS K STRITTMATTER PO BOX 15512 YORK PA 17405-1512
1	INTERNATL RSRCH ASSN D ORPHAL 4450 BLACK AVE PLEASANTON CA 94566	10	NATL INST OF STANDARDS & TECH CRMCS DIV G QUINN STOP 852 GAIITHERSBURG MD 20899
		2	DIR USARL AMSRD ARL D C CHABALOWSKI V WEISS BLDG 205 2800 POWDER MILL RD ADELPHI MD 20783-1197

NO. OF
COPIES ORGANIZATION

ABERDEEN PROVING GROUND

65 DIR USARL
AMSRD ARL WM
S KARNA
J MCCUALEY (20 CPS)
J SMITH
T WRIGHT
AMSRD ARL WM B
J NEWILL
M ZOLTOSKI
AMSRD ARL WM M
S MCKNIGHT
R DOWDING
AMSRD ARL WM MC
R SQUILLACIOTI
AMSRD ARL WM MD
E CHIN
K CHO
G GAZONAS
J LASALVIA
P PATEL
J MONTGOMERY
J SANDS
AMSRD ARL WM T
P BAKER
B BURNS
AMSRD ARL WM TA
P BARTKOWSKI
M BURKINS
W GOOCH
D HACKBARTH
T HAVEL
C HOPPEL
E HORWATH
T JONES
M KEELE
D KLEPONIS
J RUNYEON
S SCHOENFELD
H MEYER
AMSRD ARL WM TC
R COATES
T FARRAND
K KIMSEY
L MAGNESS
S SEGLETES
D SCHEFFLER
R SUMMERS
W WALTERS

NO. OF
COPIES ORGANIZATION

AMSRD ARL WM TD
T BJORKE
J CLAYTON
D DANDEKAR
M GREENFIELD
E RAPACKI
M SCHEIDLER
T WEERASOORIYA

NO. OF
COPIES ORGANIZATION

3 FRAUNHOFER-INSTITUT FÜR
KURZZEITDYNAMIK (EMI)
PROF DR K THOMA
DIPL-PHYS E STRAßBURGER
AM KLINGELBERG 1 D – 79588
EFRINGEN-KIRCHEN
GERMANY

INTENTIONALLY LEFT BLANK.